D'Hondt, S.L., Jørgensen, B.B., Miller, D.J., et al., 2003
Proceedings of the Ocean Drilling Program, Initial Reports Volume 201

12. SITE 1231[1]

Shipboard Scientific Party[2]

BACKGROUND AND OBJECTIVES

Site 1231 was selected for drilling in order to study the microbial activities and communities of the organic-poor sediments that characterize much of the world's open ocean. Before drilling at Site 1231, the nature of subseafloor microbial communities in open-ocean clays had never been assessed.

The principal objectives at this site were

1. To test by comparison with other sites drilled during this expedition whether microbial activities, microbial communities, and the nature of microbe-environment interactions are different in very organic poor open-ocean sediments than in the more organic-rich sediments of the equatorial upwelling region and the coastal upwelling region and
2. To document the microbial activities, communities, and environmental context of an expanded manganese-reducing zone in very organic poor, relatively deeply buried marine sediments.

Site 1231 is in the Peru Basin at 4827 m water depth. The lithologies, age, and many geochemical characteristics of the targeted sediments were characterized by Leg 34 studies at nearby Site 321 (Shipboard Scientific Party, 1976). The total sediment thickness at Site 321 is 115 m. The sediment is composed of 58 m of late Oligocene to Holocene clay and 57 m of iron-rich late Eocene to early Oligocene nannofossil ooze (Shipboard Scientific Party, 1976). The lower 50 m of sediment at Site 321 is rich in iron and manganese (Dymond et al., 1976). Iron and manganese accumulation rates estimated for the sediments present below 49 meters below seafloor (mbsf) are about an order of magnitude higher than those estimated for sediments above 49 mbsf (Boström et al., 1976). In analyses of six interstitial water samples, dissolved manganese was

[1]Examples of how to reference the whole or part of this volume.
[2]Shipboard Scientific Party addresses.

Ms 201IR-112

present at relatively higher concentrations in the upper 45 m of the sediment column (3.5–7.4 ppm) than in the lower 50 m (0–1 ppm) (Brady and Gieskes, 1976). Dissolved sulfate concentrations also appeared to be slightly higher in the upper 45 m (>28 mM) than in the lower 50 m (27 mM) (Brady and Gieskes, 1976). Little or no evidence for other postdepositional reactions was seen among major dissolved ions at Site 321. This finding led Brady and Gieskes (1976) to conclude that any reactions in these sediments occur at such slow rates that their chemical signature is annihilated by exchange with the top and bottom of the sediment column. Consequently, Site 1231 provided a challenging opportunity for assessing the microbial activities and communities of low-activity sediments typical of much of the open ocean.

The subsurface extent of key electron donors (hydrogen, acetate, and formate), electron acceptors with standard free-energy yields greater than that of sulfate (oxygen and nitrate), products of key metabolic reactions (dissolved iron), and other biologically important chemicals was not determined for Site 321.

PRINCIPAL RESULTS

At Site 1231, the dissolved inorganic carbon (DIC) profile hovers slightly at or below 3.3 mM for most of the sediment column. It exhibits three slight exceptions to this relative constancy: it slightly increases from 2.8 mM near the sediment/water interface, it exhibits a small peak of ~3.7 mM centered at 55 mbsf, and it declines slightly to ~3.0 mM at the sediment/basement interface. These DIC concentrations are even lower than those at Site 1225 (3.0–4.0 mM). They are much lower than the DIC concentrations observed at the other Leg 201 sites. Dissolved ammonium concentrations are also generally lower at Site 1231 than at the other Leg 201 sites. As at Site 1225, concentrations of DIC, ammonium, and alkalinity peak in the middle of the sediment column and decline toward both the sediment/ocean interface and the sediment/basement interface. The relatively low variability in the concentration profiles of these chemical species suggests that net microbial activity may be lower at Site 1231 than at any other Leg 201 site. The midcolumn peaks in these profiles and their relatively low values near both the sediment/water and sediment/basement interfaces indicate chemical exchange between the sediment and the ocean and between the sediment and the basement.

Dissolved sulfate concentrations are >28 mM at the sediment surface and decrease linearly to 27 mM near the basement. The slight total downhole decrease in sulfate concentrations suggests that Site 1231 is characterized by very low sulfate-reducing activity. Dissolved sulfide ($\Sigma H_2S = H_2S + HS^-$) is below the detection limit (0.0002 mM) throughout the entire sediment column.

Electron acceptors with higher standard free-energy yields than sulfate are present throughout most of the sediment column at Site 1231. Dissolved nitrate appears to be present in the uppermost meter and the lowermost 60 m of the sediment column (where it ranges from ≥15 µM at 114 mbsf to 2 µM at 77 mbsf). Dissolved oxygen similarly appears to be present in the top 0.6 m below the seafloor as well as the last 3.8 m of sediment above basaltic basement. The diffusion of oxygen and nitrate from the overlying ocean down into the sediment is readily predictable from deep-ocean chemistry. However, the first Leg 201 locations, Sites 1225 and 1226, provided the only previous precedent for

upward transport of nitrate (and, at Site 1225, oxygen) into deeply buried sediment from the underlying basaltic crust. As at Site 1225, the introduction of dissolved nitrate high into the sediment column at Site 1231 indicates that nitrate-utilizing microbial activity is present but may proceed at a very low rate in the site's lowermost sediments. Also as at Site 1225, the presence of dissolved oxygen and nitrate in these deepest sediments suggests that microbial activity in the underlying basalt is insufficient to strip even the scarcest preferentially utilized electron acceptors from the water that flows through the basalt.

Dissolved manganese is present from 1 to 65 mbsf at Site 1231. Concentrations steadily rise from ~17 µM at 1.4 mbsf to a local peak of 78 µM at ~17 mbsf, decline briefly by a few micromolar, and then rise to sustain highest concentrations of 120 µM from 36 to 46 mbsf. Manganese concentrations below this peak steadily decline to essentially 0 µM at 68 mbsf. A relatively broad zone of generally high but variable dissolved iron concentrations (7–36 µM) spans the interval from 1 to 30 mbsf. A very small secondary peak in dissolved iron (5 µM) is centered near 74 mbsf. Two aspects of these broad patterns run counter to the general expectation that manganese reduction occurs at shallower depths than iron reduction in marine sediments. The first aspect is the broad co-occurrence of dissolved iron and manganese from 1 to 30 mbsf. The second aspect is the presence of the maximum dissolved iron concentrations much closer than the maximum dissolved manganese concentrations to the sediment/water interface. It appears likely that rates of manganese reduction in these sediments are limited by the availability of manganese oxides that supply dissolved manganese. Rates of iron reduction may be similarly limited by the presence and solubility of the minerals that supply dissolved iron.

As at other Leg 201 sites, the downhole distribution of microbial manganese and iron reduction at Site 1231 appears to be ultimately determined by lithology and depositional history. The peak intervals of dissolved manganese production are limited to the clays that lie between 11 and 55 mbsf. The maximum manganese concentration (120 µM) is present in the yellow volcanic-rich clay of Subunit IIA (31–44 mbsf). The secondary peak (78 µM) is centered in the green diatom-rich clay of Unit I (11–30 mbsf). Dissolved iron is similarly limited to the clay-rich portions of the upper sediment column. It exhibits a sharp maximum concentration (36 µM) a few meters below the seafloor in the radiolarian and clay-rich diatom ooze of upper Unit I (0–11 mbsf). Most of the dissolved iron at Site 1231 is present in a broad maximum of 26 µM in the green clay of Unit I. Dissolved iron concentrations are consistently ≤5 µM in the nannofossil oozes that lie between 55 mbsf and the basaltic crust (114 mbsf). Dissolved manganese is consistently <1 µM over the same interval.

Although Site 1231 may be the microbially least active of the Leg 201 sites, its sediments still contain methane at concentrations of up to 15 µM. At this site, methane is limited to the upper clay-rich portion of the sediment column between 0 and 42 mbsf. This methane-bearing interval is completely within the interval of high dissolved manganese concentrations. Interestingly, this methane was only detected after prolonged incubation of headspace samples over a couple of days, whereas short 20-min incubation according to the standard Ocean Drilling Program (ODP) safety protocol showed only trace methane concentrations throughout the sediment column. The appearance of methane over time is currently interpreted as a release of sorbed methane. From sediments below 42 mbsf, no release of sorbed methane was observed and

the concentrations remained at trace levels of <0.2 µM. The relationship of this sorbed methane to current microbial activity remains unknown.

Acetate concentrations range between 1 and 14 µM at Site 1231. Formate varies between 1 and 19 µM. Concentrations of both fatty acids are lowest in the top 3 m below seafloor (1–2 µM). They are slightly higher (3–6 µM) in the nitrate-reducing zone that spans the last 50 m above basement. Acetate and formate exhibit their highest concentrations (4–14 µM and 9–19 µM, respectively) at intermediate sediment depths (25–75 mbsf and 25–80 mbsf, respectively). These broad patterns suggest that at Site 1231 fatty acid concentrations may be lower in the sedimentary intervals that include electron acceptors with the highest energy yields. Curiously, the acetate and formate concentrations at this site are generally an order of magnitude higher than concentrations in sediments of the equatorial Pacific sites but are similar to those found at the Peru margin sites and in other very active coastal marine sediments. As noted in previous site chapters, accurate understanding of the fatty acid distribution and its microbial relevance will require thorough postcruise analyses of microbial energetics in subseafloor environments.

Hydrogen concentrations are extremely high in the uppermost 35 m of the sediment column, with a peak value of 102 nM at 15 mbsf. This is the highest hydrogen concentration measured at any Leg 201 site. It exceeds the hydrogen concentrations of near-surface iron-reducing sedimentary environments by >100-fold. The zone of high hydrogen coincides with the zone of iron reduction but does not show any direct correlation with distributions of fatty acids or methane. The presence of extremely high hydrogen concentrations at the site with the lowest organic carbon mineralization rates remains unexplained at this point. From 44 mbsf down to the basaltic basement, hydrogen concentrations are, in contrast, very low (0.05–0.22 nM).

Prokaryotic cell counts were conducted on samples from throughout the sediment column at Site 1231. These data show that mean cell concentrations are generally lower at this open-ocean site than at any previously enumerated ocean drilling site. Cell concentrations exhibit a distinct local concentration peak at 10–15 mbsf, the approximate depth of the Unit I zone of iron and manganese reduction.

Experiments on major microbial processes and on enumeration of viable prokaryotes were initiated at selected depths ranging from near the seafloor to the bottom of the drilled sediment column. The studied processes include methane and acetate formation and consumption, sulfate reduction, hydrogen oxidation, and rates of cell growth. The cultivation experiments include selective growth conditions for a wide range of autotrophic and heterotrophic prokaryotes ranging from psychrophilic to thermophilic. Cultivation experiments particularly focused on manganese- and iron-reducing bacteria throughout the column. Studies of sulfate-reducing bacteria in macrofaunal burrows were also initiated. Detailed microbiological sampling targeted sediment depths of particular biogeochemical interest, such as the midcolumn reduced manganese interface and the sediment/basalt interface.

The results from six Adara tool deployments define a temperature profile composed of two distinct intervals: a linear gradient of 90°C/km from 0 to 55 mbsf and a linear gradient of 35°C/km from 55 to 115 mbsf. The sediment/water interface temperature measured by a mudline Adara tool deployment is 1.7°C. The estimated temperature at the base of the drilled sediment column (115 mbsf) is 8.6°C. Throughout

the entire drilled interval (0–121 mbsf), temperatures are in the psychrophilic range.

Trials were undertaken of two experimental tools at this site: the Davis-Villinger Temperature-Pressure Probe (DVTP-P) and the catwalk infrared (IR) camera. The single DVTP-P deployment indicated minor overpressure at 108 mbsf.

OPERATIONS

Transit to Site 1231

The 191-nmi sea voyage between Sites 1230 and 1231 lasted 18.2 hr at an average speed of 10.2 kt. A positioning beacon was deployed over the Global Positioning System coordinates of Deep Sea Drilling Project (DSDP) Site 321 in 4824.9 meters below rig floor (mbrf) water depth (precision depth recorder). Coring operations at Site 1231 are detailed in Table T1.

T1. Coring summary, Site 1231, p. 51.

Holes 1231A and 1231B

Hole 1231A was initiated at 0300 hr on 20 March 2002. When Core 201-1231A-1H returned full we could not determine the mudline, so the hole was abandoned. The first core from Hole 1231B (Core 201-1231B-1H) (0.0–3.4 mbsf; recovery = 100%) was initiated by pulling the bit ~5 m above the bit depth of Core 201-1231A-1H. Recovery established the mudline at 4824.0 mbrf. Continuous advanced hydraulic piston coring (APC) through Core 201-1231B-12H (3.4–107.9 mbsf) returned 102% recovery. Based on Leg 34 recovery at this location (Yeats, Hart, et al., 1976), we expected basement penetration at ~124 mbsf, so after a final deployment attempt of the DVTP-P at 107.9 mbsf, we drilled out the interval disturbed by the probe tip (to 109.4 mbsf) and fired Core 201-1231B-13H, which only returned 5 m of core with small chips of basalt in the core catcher. Fearing we had struck basement (some 9.5 m shallower than reported in the coring summary table for Leg 34) we deployed the extended core barrel, which immediately showed indication of hard basement (slow penetration and high, erratic torque). After 2 hr, we had advanced <3 m, so we recovered the core barrel (Core 201-1231B-14X; 114.4–117.3 mbsf), which returned only a few pieces of basalt. Having reached our basement target, we terminated Hole 1231B.

Perfluorocarbon tracer (PFT) was pumped continuously during all coring operations at Site 1231. In addition, fluorescent microspheres were deployed on Cores 201-1231A-1H and 201-1231B-1H, 2H, 6H, 12H, and 14X. The Adara temperature shoe was deployed at the mudline and at 41.4, 60.4, 88.9 and 118.9 mbsf. The DVTP-P tool was deployed after Core 201-1231B-12H at a depth of 107.9 mbsf.

Hole 1231C and 1231D

Two cores were recovered to support high-resolution paleoceanographic and paleomagnetic studies (Cores 201-1231C-1H and 2H; 0.0–15.1 mbsf). Because heavy microbiological and geochemical whole-round core sampling depleted a significant part of the recovery at Hole 1231B, we chose to recover a complete section (Cores 201-1231D-1H through 13H and 14X [0.0–121.9 mbsf; recovery = 92%]) at this site in

support of shipboard and shore-based solid-phase sampling. The Adara temperature shoe was deployed at 74.3 and 112.3 mbsf in Hole 1231D.

Still in a quandary over the offset between the depth where we encountered basement (~115 mbsf) and where the Leg 34 coring and lithostratigraphic summary reported the basement contact (124.5 mbsf), we noted an interval in the Site 321 lithostratigraphic column that reported 9.5 m (between 96.5 and 106.0 mbsf) as uncored. The sediments above and below this interval in our recovery are similar in appearance to those described in the Leg 34 site report. The time on deck between cores surrounding the reported uncored interval is recorded as 1.5 hr, which was similar to our wireline time in this water depth, suggesting little time was spent on drilling without coring. The operations section of the Site 321 chapter does not report an uncored interval, and the reported depths between mudline depth and basement contact differ by 114.5 m. We can only surmise that there was a recording error in the coring summary table that was accounted for in the lithostratigraphic column as a coring gap, but that the basement contact at Site 321 is at the same depth as at Site 1231.

Hole 1231E

Our final operation for Leg 201 was recovery of a complete section to sample specific intervals for high-resolution microbiology and geochemistry. Cores 1H through 14H (0.0–119.0 mbsf; recovery = 100%) ended with a final penetration into basement. The Adara temperature shoe was deployed at 98 mbsf. Operations for Leg 201 ended when the bit passed through the rig floor at 1600 hr on 23 March, and we began our ~5-day transit to Valparaiso, Chile. We arrived at the pilot station in Valparaiso at 0716 hr on 29 March and the first line ashore at 1120 hr officially ended Leg 201.

LITHOSTRATIGRAPHY

At Site 1231, we recovered a 121.9-m-thick Holocene through late Eocene age sequence of mostly biogenic and clay sediments from the Peru Basin. The proposed lithostratigraphy is based on three holes that penetrated the entire sedimentary section and reached the top of the oceanic basement (Holes 1231B, 1231D, and 1231E). Based on observations of lithology, sediment color, textures (visual core description), smear slide analysis, and color reflectance, sediments from Site 1231 were subdivided into three lithostratigraphic units (Fig. F1). X-ray diffraction (XRD) and measurements of magnetic susceptibility, density, and natural gamma radiation (see "Physical Properties," p. 18) were also used to detect lithologic and sedimentologic changes. As Site 1231 is located in close proximity (within 100 m of the reported coordinates) of Leg 34 Site 321, the age framework presented in this chapter follows the chronostratigraphic observations of the Leg 34 Shipboard Scientific Party (Shipboard Scientific Party, 1976) and the calcareous nannofossil biostratigraphy for Site 321 proposed by Blechschmidt (1976) and modified after Berggren et al. (1995).

F1. Lithostratigraphic summary, p. 28.

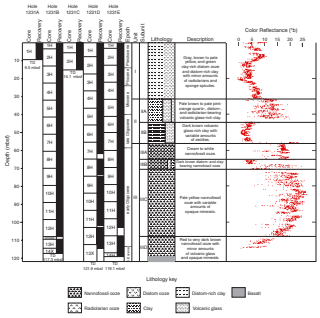

Description of Lithostratigraphic Units

Unit I

Interval: 201-1231A-1H-1 through 1H-CC; 201-1231B-1H-1 through 4H-7, 20 cm; 201-1231C-1H-1 through 2H-CC; 201-1231D-1H through 4H-4, 80 cm; and 201-1231E-1H-1 through 4H-CC.
Depth: 0–9.5 mbsf (Hole 1231A); 0–31.1 mbsf (Hole 1231B); 0–15.1 mbsf (Hole 1231C); 0–32.1 mbsf (Hole 1231D); and 0–31.5 mbsf (Hole 1231E)
Age: Miocene–Pleistocene

Unit I consists of gray-brown to pale yellow clay-rich diatom ooze and diatom-rich clay with minor amounts of radiolarians, sponge spicules, and trace amounts of quartz, plagioclase, glauconite, and pyrite (e.g., XRD Sample 201-1231B-2H-6, 45–46 cm) (see **"Mineralogy,"** p. 10). The uppermost 60–70 cm is red to brown and is characterized by slightly darker laminae (Fig. **F2A**). Large black sulfide accumulations are concentrated around 1.0 mbsf (Fig. **F2B**). Below 0.6 mbsf, sediments of Unit I are generally gray to pale gray and show weak banding either due to the presence of green to gray layers or dark gray to black pyrite-rich laminae. Burrows are common from 0 to 12 mbsf; many of them are open and some are outlined by dark alteration rims. Between 11 and 12 mbsf (Sections 201-1231B-2H-6 and 201-1231D-2H-3), the color of the sediment changes from gray to greenish gray and the sediments are richer in siliciclastic material. The average composition is diatom- and silt-rich clay. This change is also highlighted by negative shifts in both chromaticity (Fig. **F1**) and magnetic susceptibility (see **"Physical Properties,"** p. 18). Below this transition, dark pyrite-rich zones are more abundant and are present concentrated in distinct layers and around burrows (Fig. **F2C**). The bottom of Unit I is marked by a sharp and prominent change in sediment color from orange-yellow to brown. This change in sediment color coincides with a shift in color reflectance (Fig. **F1**) and a positive excursion toward higher natural gamma radiation values (see **"Physical Properties,"** p. 18). It is worth noting that at about the same depth the iron content of interstitial waters drops very to close to zero (see **"Biogeochemistry,"** p. 12).

F2. Site 1231 features, p. 29.

Unit II

Interval: 201-1231B-4H-7, 20 cm, through 7H-3; 201-1231D-4H-4, 80 cm, through 7H-1, 30 cm; and 201-1231E-4H-CC through 7H-5, 20 cm.
Depth: 31.1–55.4 mbsf (Hole 1231B); 32.1–55.6 mbsf (Hole 1231D); and 31.5–56.5 mbsf (Hole 1231E)
Age: late Oligocene–Miocene

Sediments of Unit II are characterized by relatively higher amounts of clay and small to moderate amounts of volcanic glass. Biogenic components such as diatoms, radiolarians, and foraminifers are rare or absent. The dominant color of the upper 13 m of this unit is brown-orange to dark yellow, whereas the lower 11 m of the unit is brown to dark brown. This color change coincides with compositional variations of the sediment as well as with shifts in some of the physical properties (magnetic susceptibility, natural gamma radiation, and grain density; see **"Physi-**

cal Properties," p. 18). These variations caused us to subdivide Unit II into two subunits.

Subunit IIA

Interval: 201-1231B-4H-7, 20 cm, through 6H-2; 201-1231D-4H-4, 80 cm, through 6H-2; and 201-1231E-4H-CC through 6H-2
Depth: 31.1–44.0 mbsf (Hole 1231B); 32.1–44.6 mbsf (Hole 1231D); and 31.5–44.0 mbsf (Hole 1231E)

Subunit IIA consists of pale brown to pale pink-orange quartz-, diatom-, and radiolarian-bearing volcanic glass–rich clay. This main lithology alternates with 10- to 40-cm-thick darker layers with more abundant sulfide minerals. The abundance of trace fossils varies from low to moderate and is generally higher in the darker intervals (Fig. F2D). The upper boundary of this subunit is marked by a color change from green to pale brown. This color change coincides with a positive shift in chromaticity values and natural gamma radiation. The transition to Subunit IIB includes a drastic shift of sediment color and a minor compositional change toward zeolite- and volcanic glass–rich clay.

Subunit IIB

Interval: 201-1230B-6H-3 through 7H-4, 20 cm; 201-1231D-6H-6, 80 cm, through 7H-1; and 201-1231E-6H-3 through 7H-5, 20 cm
Depth: 44.4–55.5 mbsf (Hole 1231B); 44.6–55.6 mbsf (Hole 1231D); and 44.0–56.5 mbsf (Hole 1231E)

The top of Subunit IIB is marked by a change in sediment color from pale orange (Subunit IIA) to dark brown. This change corresponds to a major color reflectance shift (Figs. F1, F2D). This subunit also includes a portion of the section characterized by increased grain density, magnetic susceptibility, and natural gamma radiation values (see also "Physical Properties," p. 18). The main lithology of Subunit IIB is dark brown volcanic glass–rich clay with variable amounts of zeolite (e.g., XRD Sample 201-1231B-7H-1, 60–61 cm) (see "Mineralogy," p. 10) and trace amounts of nannofossils. Signs of bioturbation are visible in the form of several burrows composed of nannofossil-rich clay. This nannofossil-rich clay was most likely transported from the overlying subunit by biological activity. The bottom of Subunit IIB has a sharp contact with the white nannofossil ooze of Unit III and corresponds to a major shift in color reflectance (Fig. F1). This boundary also coincides with decreases in magnetic susceptibility, natural gamma radiation, and porosity, as well as increases in *P*-wave velocity, thermal conductivity, and bulk density (see also "Physical Properties," p. 18). The depth of this boundary is also in close proximity to a small shift of interstitial water sulfate concentrations (see "Biogeochemistry," p. 12).

Unit III

Interval: 201-1230B-7H-4, 20 cm, through 14X; 201-1231D-7H-1 through 13X-3; and 201-1231E-7H-5, 20 cm, through 14H-CC
Depth: 55.5–114.4 mbsf (Hole 1231B); 55.6–114.4 mbsf (Hole 1231D); and 56.5–119.1 mbsf (Hole 1231E)
Age: late Oligocene to late Eocene

Unit III consists of white to dark brown nannofossil ooze with varying amounts of foraminifers, manganese and iron oxides, volcanic glass, cal-

cite grains, and zeolites. Sediment color changes with increasing depth. In general, darker hues are more common in proximity to the basement. As clay is only present in minor amounts, color changes from whitish to brownish hues are attributed to varying amounts of oxide minerals. These color changes, most of which can be correlated to changes in physical properties, justified subdivision into four subunits (Fig. F1).

Subunit IIIA

Interval: 201-1231B-7H-4, 73 cm, through 8H-4; 201-1231D-7H-1, 30 cm, through 8H-1, 25 cm; and 201-1231E-7H-5 through 8H-4, 105 cm
Depth: 55.5–65.6 mbsf (Hole 1231B); 55.6–65.0 mbsf (Hole 1231D); and 56.5–65.6 mbsf (Hole 1231D)

Sediments in Subunit IIIA are cream to white and are composed of almost pure nannofossil ooze (upper section of Fig. F2E). The nannofossil assemblage is strongly dominated by *Discoaster* sp. No primary sedimentary textures, such as laminations or burrows, were observed. However, the homogeneous aspect of the sediment might be the effect of pervasive bioturbation. The upper and lower boundaries of the subunit coincide with increases in grain density, bulk density, and *P*-wave velocity. They can also be correlated with negative excursions in porosity and natural gamma radiation (see **"Physical Properties,"** p. 18). Unlike the sediments from the units above, X-ray diffractograms from Subunit IIIA show high intensities, which indicate high concentrations of mineral phases (calcite) and a low abundance of amorphous material (e.g., XRD Sample 201-1231B-8H-4, 60–61 cm) (see also **"Mineralogy,"** p. 10). The lower boundary of Subunit IIIA corresponds to an abrupt change in color (Fig. F2E), and it also coincides with the depth interval at which the interstitial water manganese approaches concentrations near zero (see **"Biogeochemistry,"** p. 12).

Subunit IIIB

Interval: 201-1231B-8H-4, 73 cm, through 9H-1, 70 cm; 201-1231D-8H-1, 25 cm, through 8H-5; and 201-1231E-8H-4, 105 cm, through 9H-3, 20 cm
Depth: 65.6–70.5 mbsf (Hole 1231B); 65.0–74.8 mbsf (Hole 1231D); and 65.6–72.7 mbsf (Hole 1231E)

Subunit IIIB is ~5 m thick and consists of dark brown diatom- and clay-bearing nannofossil ooze that contains variable amounts of opaque minerals and zeolites (e.g., XRD Sample 201-1231B-8H-5, 60–61 cm) (Fig. F2E). Both the top and the bottom of this subunit correspond to prominent shifts in magnetic susceptibility and natural gamma radiation (see **"Physical Properties,"** p. 18). A dark sulfide layer is present a few centimeters below the upper boundary (Fig. F2E). The sediment is characterized by alternating brown and dark brown layers that show signs of moderate to strong bioturbation (mostly of *Planolites* type). Both the observed color change and the presence of a sulfide layer near the top of this subunit may be related to a drop in interstitial water manganese concentrations (see **"Biogeochemistry,"** p. 12).

Subunit IIIC

Interval: 201-1231B-9H-1, 70 cm, through 12H-CC; 201-1231D-8H-5 through 12H-5, 100 cm; and 201-1231E-9H-3, 20 cm, through 13H-1

Depth: 70.5–107.9 mbsf (Hole 1231B); 74.3–109.8 mbsf (Hole 1231D); and 72.7–109.0 mbsf (Hole 1231E)

The dominant lithology of Subunit IIIC is orange to pale yellow nannofossil ooze with variable amounts of foraminifers and opaque or semiopaque minerals. Abundance of trace fossils is low to moderate. The only notable textural features of these otherwise homogeneous sediments are scattered lighter- and darker-colored bands present throughout the subunit. However, as already noted in Subunit IIIA, the homogeneous appearance of the sediments may be the result of intensive bioturbation. In all holes, the lower boundary of this subunit is not a sharp contact but rather a gradual transition toward darker red and brown sediments.

Subunit IIID

Interval: 201-1231B-13H-1 through 13H-CC; 201-1231D-12H-5, 100 cm, through 13X-CC; and 201-1231E-13H-2 through 14H-CC

Depth: 107.9–114.4 mbsf (Hole 1231B); 109.8–114.4 mbsf (Hole 1231D); and 109.0–119.1 mbsf (Hole 1231E)

The last 5 to 7 m of sediment directly above oceanic basement is characterized by red to very dark brown nannofossil ooze of mostly calcitic composition (e.g., XRD Sample 201-1231B-13H-3, 132–133 cm). Sediments contain up to 5% of dark brown semiopaque mineral grains of unidentified composition (presumably oxides of manganese and iron). Alternation between darker and lighter layers is the only common sedimentary feature for this subunit. The basalt/sediment contact was encountered at 114.4 mbsf in Holes 1231B and 1231D and at 119.1 mbsf in Hole 1231E. Fragments of basalt were recovered in Holes 1231B (Section 201-1231B-14X-CC), 1231D (Section 201-1231D-13X-CC), and 1231E (Section 201-1231E-14H-3) and were completely consumed by microbiological sampling.

Mineralogy

XRD mineralogic analyses were performed on 27 samples collected from the three units recognized at Site 1231. Seven main mineral species were found: calcite, plagioclase, quartz, glauconite, clay minerals, pyrite, opal-A, and zeolite (philipsite). In general, their distribution and relative amounts in the mineralogic assemblage reflects the lithologic variations in Site 1231 sediments.

XRD diffractograms from Unit I, and in particular from Unit II, are characterized by very low intensities, which are caused by the presence of large percentages of nondetectable amorphous components in the sediment (e.g., volcanic glass). Low to trace amounts of quartz, opal-A, pyrite, glauconite, plagioclase, and clay minerals compose the mineralogic assemblage of most of the samples from these two units. In Unit I, quartz and opal-A are slightly more abundant. Most of the samples collected from Unit II contain zeolites, which appear to be more abundant in Subunit IIB, where they can comprise up to 15% of the sediment. Zeolite mineral grains commonly show twinning and have a cloudy appearance, which causes almost isotropic behavior under cross-polarized light. In the same subunit, volcanic glass, most likely the precursor for the zeolites, is present in concentrations as high as 5%.

Calcite was the main and, in most samples, the only detectable mineral in Unit III. XRD intensities from this unit are much stronger than

in Units I and II, thus suggesting a higher abundance of crystalline phases and a much smaller percentage of amorphous components. Calcite, which is clearly of biogenic origin, shows higher XRD intensities in the white and orange nannofossil oozes of Subunits IIIA and IIIC. In contrast, calcite is less abundant in the brown sediments of Subunit IIIB and is present mixed with quartz, plagioclase, and zeolites.

Thin Section

Reddish brown basalt was recovered in Section 201-1231B-14X-1, and a small piece was archived for postcruise description (see **"Site 1231 Thin Section"**) and geochemical analysis. In thin section, this sample is much different than the basalt recovered from Site 1226 in that there is no olivine and only rare plagioclase phenocrysts. In addition, iron-titanium oxide in the groundmass is much more abundant in the sample from Site 1231. Clinopyroxene microphenocrysts are rare but are present as glomerocrysts with small plagioclase laths. Smectite is the most common alteration phase filling vesicles and microfractures, with rare calcite and some palagonite. Compositionally, this sample is a iron-titanium basalt (Table **T2**) with a similar composition to the average reported composition for samples from DSDP Site 321 (Bunch and LaBorde, 1976).

T2. Basalt compositions, p. 53.

Summary

At Peru Basin Site 1231, a ~120-m-thick section of Pleistocene through late Eocene age mostly biogenic and clayey sediments was divided into three lithostratigraphic units. Unit I consists of Pleistocene to Miocene gray and brown to pale yellow clay-rich diatom ooze and diatom-rich clay with minor amounts of radiolarians, sponge spicules, and trace amounts of quartz, plagioclase, glauconite, and pyrite. Unit II (late Oligocene to Miocene) is characterized by clay-rich sediments poor in biogenic components. Subunit IIA is composed of pale brown to pale pink-orange variably bioturbated, quartz-, diatom-, and radiolarian-bearing volcanic glass–rich clays. Subunit IIB consists of dark brown volcanic glass–rich clay with variable amounts of zeolite and trace amounts of nannofossils. Unit III (late Oligocene to late Eocene), which directly overlies the oceanic basement, is composed of nannofossil ooze. Within this unit, four subunits were recognized. Subunit IIIA is composed of cream to white nannofossil ooze. Subunit IIIB is a brown to dark brown nannofossil ooze. Subunit IIIC is orange to pale yellow nannofossil ooze with variable amounts of foraminifers. Subunit IIID is composed of red to dark brown nannofossil ooze rich in foraminifers and opaque minerals, which directly overlies the oceanic basement.

Seven mineral groups characterize the mineralogic assemblage of Site 1231 sediments: calcite, plagioclase, quartz, glauconite, clay minerals, pyrite, opal-A, and zeolite (phillipsite). XRD diffractograms from Unit I, and in particular from Unit II, are characterized by very low intensities caused by the presence of large percentages of nondetectable amorphous components. Most samples collected from Unit II contain zeolite. Calcite was the dominant mineral in all samples collected from Unit III.

BIOGEOCHEMISTRY

The interstitial water (IW) sampling strategy at Site 1231 was similar to that at previous Leg 201 sites. A moderately high resolution of three samples per core in Hole 1231B was followed by more detailed sampling in Hole 1231E, targeting intervals of particular geochemical relevance. We collected a total of 67 IW samples from Holes 1231B and 1231E. Geochemical data are consistent with very low microbial activity in lithostratigraphic Units I and II and extremely low activity in Unit III (see "Lithostratigraphy," p. 6). In addition, there is evidence of the upward advection of nitrate- and oxygen-containing fluid through the section from the basement.

Alkalinity and DIC have very similar profiles downhole (Fig. F3A, F3B; Table T3). The total amplitudes of alkalinity and DIC variations at Site 1231 are similar to those from Site 1225 and are significantly lower than those from Site 1226. Alkalinity increases from 2.9 mM in the 0- to 0.10-mbsf interval to 3.6 mM at 26.8 mbsf, then is uniform until reaching a small peak of 4.0 mM at 55.3 mbsf. Concentrations decrease gradually to 2.9 mM at the bottom of Hole 1231B. The range in alkalinity values is 1.1 mM. DIC values increase from 2.9 mM in the 0- to 0.10-mbsf interval to 3.4 mM at 16.2 mbsf, then are uniform until reaching a small peak of 3.7 mM at 55.3 mbsf. DIC concentrations then decrease gradually to 2.9 mM at the bottom of Hole 1231B. The range in DIC values is 0.8 mM.

Oxygen measurements were conducted by microelectrode (see "Biogeochemistry," p. 9, in the "Explanatory Notes" chapter) on Cores 201-1231D-1H, 12H, and 13H (Table T4). Oxygen was detected in the upper 0 to 60 cm of Core 201-1231D-1H and decreased to background levels below that depth interval. The relatively deep penetration of oxygen into the upper 60 cm of the hole is consistent with the low microbial activity of the site. Oxygen was also detected in Core 201-1231D-13H and the bottom section of Core 12H, decreasing with distance above basement, with the shallowest depth of measurable oxygen being 3.8 m from the bottom of the hole. Although these microelectrode data are semiquantitative, they do indicate that oxygen is present in the lowermost section. This oxygen is presumably transported from underlying crustal water.

Concentrations of dissolved nitrate were determined in 23 IW samples from Holes 1231B and 1231E (Table T3; Fig. F3C). Concentrations up to ~18 µM were detected near the bottom of Holes 1231B and 1231E. This finding is similar to observations at Site 1225 and may reflect fluid flow in the basement and possibly in the lower sediment column at Site 1231. A maximum nitrate concentration of 39.3 µM was measured at a depth of 10 cm in Hole 1231E, slightly higher than the maximum concentration of 33.1 µM measured at 0.37 mbsf at Site 1225. Dissolved nitrate was undetectable in Section 201-1231B-5H-5 at 39.25 mbsf and increased gradually with depth along a smooth gradient in Hole 1231B. High-resolution sampling in Hole 1231E revealed a more erratic but still downward-increasing profile of dissolved nitrate with depth. No obvious cause could be identified for the offset between the two profiles from the lower sections of Holes 1231B and 1231E (located ~20 m apart).

The high-resolution dissolved manganese profile (Fig. F3D) shows a steep increase in manganese concentrations from <1 µM near the sediment/water interface to 60 µM at ~6 mbsf. After rising less steeply to 26

F3. Dissolved species in IW, p. 32.

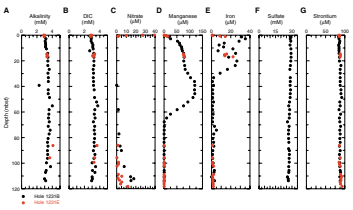

T3. Dissolved species in IW, p. 55.

T4. Oxygen by microelectrode, p. 57.

mbsf, manganese concentrations increase to 119 µM at ~36 mbsf and level off until ~47 mbsf. Dissolved manganese then declines to 0.28 µM at ~69 mbsf (Sample 201-1231B-8H-5, 135–150 cm). Concentrations remain <0.80 µM from this depth to the base of the hole at 119 mbsf. The dissolved manganese profile differs from those at the other Leg 201 sites by having a broad concentration peak in the upper 60 m of the core. This peak probably results from the microbial reduction of manganese oxide phases. As at Site 1226, the overall dissolved manganese profile may reflect sediment composition and the burial history of authigenic manganese oxides.

The dissolved iron profile (Fig. F3E) can be divided into two main zones. From just below the sediment/water interface to ~35 mbsf, iron concentrations are consistently high (3–35 µM), although, as at Sites 1225 and 1226, with considerable scatter. Dissolved iron concentrations then remain <3 µM to the bottom of the hole, except for a small peak of 5 µM centered at 74 mbsf. Microbial reduction of iron oxides probably occurs in the upper 35 mbsf; the high iron concentrations maintained over a broad zone because of the absence of dissolved oxygen and sulfides. Following work at Site 1226, a possible explanation for the variability in dissolved iron concentrations was the inclusion of solid, iron-rich particles <0.10 µm in size (e.g., magnetite) into some interstitial water samples. To address this possibility, a series of closely spaced samples from Hole 1231E were passed through 0.45-µm (standard) and 0.02-µm filters. However, iron concentrations for all of these dual analyses are identical within analytical precision (Table T5). If solid iron contributes to the variation in dissolved iron, these particles are <0.02 µm in diameter.

T5. Iron passed through two filters, p. 58.

Dissolved sulfate concentrations decrease nearly linearly from near seawater concentration at the sediment surface (28.9 mM) to 26.6 mM at 113.75 mbsf (Table T3; Fig. F3F). Slight negative inflections of ~0.7 mM from the linear trend fall close to the lower boundaries of lithostratigraphic Unit II and Subunit IIIA (56 and 65 mbsf, respectively). Two end-member scenarios can be invoked to explain the profile: (1) sulfate is reduced at a very low rate within the sediment column or (2) water depleted in sulfate relative to seawater is flowing through the basement.

Dissolved strontium concentrations (Fig. F3G) show little downhole variance, averaging 87.4 µM with a standard deviation of 1.9 µM. Dissolved lithium concentrations (Fig. F3H) also change only subtly between the seafloor and basement. Lithium concentrations are significantly higher than seawater value in the uppermost sediment (34 µM at 0 mbsf), decrease to 25 µM by ~5 mbsf, and remain between 25 and 29 µM until ~100 mbsf. Below this depth, lithium increases erratically to 40.3 µM ~5 m above basement. Concentrations of barium range between 0.4 and 1.4 µM from 1 to 10 mbsf. Above and below this interval, dissolved barium is <0.4 µM (Table T3; Fig. F3I).

Dissolved sulfide ($\Sigma H_2S = H_2S + HS^-$) concentrations are below the detection limit (<0.0002 mM) in all samples analyzed at Site 1231 (Table T3; Fig. F3J).

We analyzed the concentrations of acetate and formate in 12 IW samples from Hole 1231B (Table T3; Fig. F3K, F3L). With the exception of Site 1230, concentrations were generally higher than those at other Leg 201 sites and span a range from 1.3 to 13.5 µM (acetate) and 1.5 to 19.2 µM (formate). The concentrations of acetate and formate are low at the top and bottom of the cored interval, with a broad peak in concentration between 20 and 80 mbsf.

Hydrogen incubations were conducted on 13 samples from Hole 1231B (Table T6). Calculated interstitial fluid concentration of the incubated sediments is shown in Figure F3M. The hydrogen concentrations in the upper 25 m at Site 1231 range from 29 to 102 nM and are the highest recorded during Leg 201. The concentrations measured at 28 mbsf and below are among the lowest. The hydrogen profile is very similar in structure to the dissolved iron profile from Hole 1231B. All incubations were conducted at 4°C. Site 1231 exhibited the lowest and highest hydrogen concentrations of all the sites examined during Leg 201. Concentrations at depths shallower than 43.8 mbsf rose from 6.6 to 102 nM, whereas at greater depths concentrations were between 0.04 and 0.22 nM.

T6. Hydrogen concentrations, p. 59.

Determination of methane concentrations led to two main observations. First, methane concentrations obtained according to the ODP standard safety protocol are extremely low throughout the sediment column and are analytically indistinguishable from results obtained at Site 1225 from the 20-min and 24-hr extraction procedures (Table T7; see also "Gas Analyses," p. 11, in "Biogeochemistry" in the "Explanatory Notes" chapter for details on analytical procedure). Second, following prolonged extraction, methane yields from the upper 43 mbsf increased significantly, reaching concentrations >15 µM (Fig. F3N). At the transition to lithostratigraphic Subunit IIB (44 mbsf), methane concentrations abruptly decline to trace levels. The mechanism underlying the binding of methane to the sediment and its distribution in the fluid and solid phase has to be resolved in future work, but our observations are consistent with adsorption of methane on sediment particles.

T7. Methane concentrations, p. 60.

Ammonium concentrations increase steeply in the upper 5 m of Hole 1231B and reach a maximum of 36 µM at 20 mbsf (Table T3; Fig. F3O). Ammonium declines steadily below this maximum toward the bottom of Hole 1231B, with concentrations of only 0.6–1.2 µM measured at 113.7 mbsf. The overall shape of the profile reflects higher metabolic activity in the uppermost ~20 mbsf of the section.

Phosphate concentrations rise to a maximum of 11 µM at 6.2 mbsf and then decline gradually to fairly constant low values of ~1–2.5 µM in the lower two-thirds of the hole (Fig. F3P; Table T3).

Maximum silica concentrations are present in the top 30 mbsf and reach 688 µM (Table T3; Fig. F3Q). This peak coincides with a high content of fine-grained biogenic silica (opal-A) in lithostratigraphic Unit I (see "Lithostratigraphy," p. 6). In Unit II, the biogenic silica is diluted by a higher abundance of siliciclastic silt and clay. In Unit II the presence of zeolites has been detected visually and by XRD (see "Mineralogy," p. 10, in "Lithostratigraphy"). These zeolites may be a sink for dissolved silica. In the nannofossil ooze of Unit III, the silica is uniformly distributed with concentrations between 300 and 350 µM.

Chloride concentrations are indistinguishable from bottom seawater values near the sediment/water interface and monotonically increase by 2.8% to a depth of 12.2 mbsf (Table T3; Fig. F3R). This trend is due to the upward transport of chloride into low-salinity interglacial seawater. The depth of intrusion of the low-salinity interglacial signature is consistent with an upward advection of ~0.2 cm/yr. A number of other measurements are also consistent with upward advection. These include the nearly invariant strontium profile, the external interval of dissolved nitrate and oxygen in the lower part of the section, and an indication of overpressure at the base of the hole (see "Downhole Tools," p. 25)

MICROBIOLOGY

Microbiological sampling at Site 1231 covered both the iron- and manganese-rich zones in the upper half of the sediment column (0–68 mbsf) and the deeper sediment layers that are depleted of dissolved reduced metal ions (68–118 mbsf). In Hole 1231B, each core of the sediment column was sampled in at least two sections. One core per section was sampled for molecular microbiological analyses (deoxyribonucleic acid [DNA] and fluorescence in situ hybridization–secondary ion mass spectrometry [FISH-SIMS]), measurements of activity (sulfate reduction rates, hydrogen concentration and turnover, methanogenesis, acetate turnover, and thymidine incorporation), bacterial lipid biomarkers, adenosine triphosphate, and iron/manganese/sulfur solid phases. A second core section was sampled exclusively for iron/manganese/sulfur solid-phase analysis (Cores 201-1231B-1H through 13H) (see Fig. F4). In addition, selected depths were chosen for microbial enrichment and cultivation studies (Fig. F4)

The basalt/sediment interface at the bottom of Hole 1231D (Section 201-1231D-13H-CC; 114.35–114.7 mbsf) was sampled for DNA and biomarker analysis and microbial enrichments from sediment and basalt.

Sampling in Hole 1231E focused on intervals that had not been sufficiently sampled in Hole 1231B. These intervals were identified after the depth profiles of dissolved manganese and iron became available (Figs. F5, F3). Whole-round core (WRC) samples for enrichments of manganese(IV)- and iron(III)-reducing bacteria and some high-resolution samples for DNA analysis were taken. Several 1.5-m core sections showed conspicuous color gradients that corresponded to pronounced lithostratigraphic changes (see "Description of Lithostratigraphic Units," p. 7, in "Lithostratigraphy"). Section 201-1231E-6H-2 (42.5–44.0 mbsf) changed from orange-yellow volcanic glass–rich clay at the top to brown clay at the bottom. Section 201-1231E-7H-4 (55.0–56.5 mbsf) changed from dark brown clay at the top to cream-colored nannofossil ooze at the bottom. Section 201-1231E-8H-4 (64.5–66 mbsf) was bisected by a sharp discontinuity at ~90 cm (65.4 mbsf), where the cream-colored nannofossil ooze at the top turned abruptly into chocolate-brown diatom-bearing clay at the bottom. In all three cases, DNA, biomarker, and enrichment samples were taken twice, from both ends of the core sections (Fig. F5).

Total Prokaryotic Cell Enumeration

Samples (1 cm^3) for total prokaryotic cell enumeration were taken during core processing in the 4°C refrigerator from Holes 1231B (15 samples between the near surface and 113.1 mbsf), and 1231E (20 samples between 20 and 118.7 mbsf). Four depths of specific interest (~25, 53, 67, and 78 mbsf) identified by chemical profiles in Hole 1231B were sampled at high spatial resolution in Hole 1231E. All but the deepest sample (Sample 201-1231E-14H-3, 25–30 cm) from Hole 1231E were stored for shore-based processing.

Prokaryotes were present in all samples studied to the depth of 118.7 mbsf (Fig. F6). The highest number of prokaryotes, 1.72×10^8 cells/cm^3, was found near the surface (Sample 201-1231B-1H-1, 0–1 cm). The lowest number was found at 81.64 mbsf, with 1.38×10^5 cells/cm^3 (Sample 201-1231B-10H-2, 74–80 cm), was 1250-fold less than at the surface.

F4. Subsampling for MBIO, Hole 1231B, p. 35.

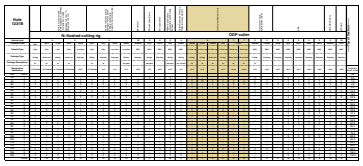

F5. Subsampling for MBIO, Hole 1231E, p. 36.

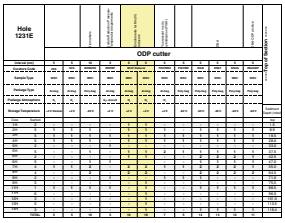

F6. Prokaryotic cells enumerated, p. 37.

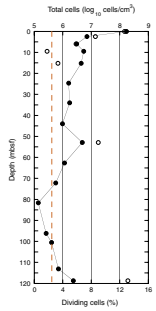

The overall depth profile of cell numbers per cubic centimeter (Fig. F7) follows a trend observed at other ODP sites (Parkes et al., 1994), although there are some substantial deviations. The sediment at Site 1231 is divided into an upper section of clay-rich sediment that overlies a nannofossil ooze (see **"Description of Lithostratigraphic Units,"** p. 7, in "Lithostratigraphy"). To a great extent, the prokaryotic cell profile mirrors the sedimentological change with considerably reduced numbers in the nannofossil ooze. In the upper 50 m, the data follow the lower prediction limit closely; however, small but significant (F-value = 7.21; degrees of freedom = 3 and 8; $P < 0.05$) increases in cell numbers occur at 9.45 and 15.23 mbsf (Samples 201-1231B-2H-5, 5–10 cm, and 201-1231B-3H-2, 83–89 cm). At 52.9 mbsf (Sample 201-1231B-7H-2, 50–56 cm), there is a substantial and significant (F-value = 12.66; degrees of freedom = 2 and 6; $P < 0.02$) increase in cell number by a factor of 5 to 4.8×10^6 cells/cm^3. Below this depth, cell numbers decrease rapidly to a minimum of 1.38×10^5 cells/cm^3 at 81.64 mbsf. This was the lowest count determined during Leg 201 and was below the limit where reliable counts are possible. The detection limit is based on calculations for a single membrane filter, and for each sample three replicate filters are used to provide a measure of variability. Where a zero count occurs, as it did in this case, the prokaryote population is estimated by combining all of the data from the three membranes and treating it as one subsample. This provides the only possible estimate of the population size in such samples but does not allow any measure of variability.

Below this depth, prokaryotic cell concentrations seem to increase; however, this may not be true, as with the exception of the deepest sample prokaryote populations in the three samples between 96.2 and 113.1 mbsf are around the detection limit. They all have large variances, and there is no statistically significant difference between them. This situation may be clarified with additional shore-based enumeration when additional subsamples can be counted, thus reducing sample variability.

The deepest sample at 118.7 mbsf had similar prokaryotic cell numbers to those at 62.64 mbsf. The reasons for this unexpected increase in cell numbers are not clear. However, this sample was very different from others higher in the sediment column in being adjacent to the basement and containing basaltic fragments.

Two increases in cell numbers occur at ~10–15 mbsf and again at ~53 mbsf. These two depths are near the upper and lower boundaries for methane concentrations found only in the upper sediments at this site. Additionally, the lower increase in prokaryotic cell counts is located near a small but significant decrease in interstitial water sulfate concentrations (see **"Biogeochemistry,"** p. 12). This suggests that enhanced bacterial activity, albeit at a low level, is occurring at this site.

Numbers of dividing cells (suggested as an index of growth activity) are typically <10% of the total count. As expected, dividing cells, as a percentage of the total count, are high near the surface (Fig. F6). They then decrease rapidly to ~1.8% at 9.5 mbsf. Below 15 mbsf, only two depths (52 and 118.7 mbsf) gave reliable enumeration of dividing cells of 9%–13%. At all other depths, the percentages of dividing cells were either zero or the total cell population was so low that determining the percentage of dividing cells became highly variable and unreliable and so are not reported here.

The nature of the sediments at this site made direct counting more problematic than usual because the presence of manganese oxide in the sediments produced flocculent material that blocked filter membranes.

F7. Total prokaryote profile, p. 38.

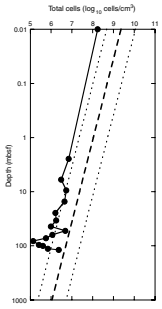

Hence, where normally subsamples of 15–40 µL can be processed, subsample size was occasionally restricted to 5 µL at Site 1231. Consequently, the detection limit increased to 4×10^5 cells/cm^3; thus, counting sensitivity decreased.

Contamination Tests

While drilling cores for microbiology, the potential for contamination with bacteria from the surface is highly critical. Contamination tests were continuously conducted using solutes (PFT) or bacterial-sized particles (fluorescent microspheres) to check for the potential intrusion of drill water from the periphery toward the center of cores and thus to confirm the suitability of the core material for microbiological research. We used the chemical and particle tracer techniques described in ODP *Technical Note* 28 (Smith et al., 2000). Furthermore, the freshly collected cores were visually examined for possible cracks and other signs of disturbance by observation through the transparent core liner. Core sections observed to be disturbed before or after subsampling were not analyzed further. Such disturbance phenomena are critical to the integrity of the core material and therefore also to its usefulness for microbiological studies.

Perfluorocarbon Tracer

The PFT was injected continuously into the drilling fluid during drilling of Holes 1231B and 1231D (see **"Perfluorocarbon Tracer Contamination Tests,"** p. 26, in "Microbiological Procedures and Protocols" in "Microbiology" in the "Explanatory Notes" chapter). PFT sampling focused on microbiology cores and especially on sections that were used for slurry preparation and cultivations. To compare PFT concentrations in the center of a core to PFT concentrations at the periphery of the same core, a 5-cm^3 subcore sample was taken adjacent to the core liner and two 5-cm^3 subcores were taken from the center. Whenever possible, the samples were taken directly on the catwalk and capped away from nearby cores because the PFT content of catwalk air under these conditions was usually negligible.

Low levels of potential seawater contamination (<0.05 µL seawater/g sediment; average = 0.023 µL seawater/g sediment) (Table **T8**) were found for the center portions of all tested cores of Holes 1231B and 1231D, including the core catcher from Core 201-1231D-13X. The outer portions of all tested cores had substantially higher levels of PFT, and therefore, higher potential seawater contamination.

T8. Seawater contamination based on PFT, p. 61.

Of the four slurry samples taken from Site 1231 (Table **T9**), none showed high concentrations of PFT that suggest potential prokaryotic cell contamination from seawater drilling fluid.

T9. Potential contamination of slurries based on PFT, p. 62.

Assuming 5×10^8 prokaryotic cells/L surface seawater, each 0.1 µL of seawater contamination may represent as many as 50 contaminating cells if the sediment is permeable enough to allow cells to travel with the PFT.

Particulate Tracer

Fluorescent microspheres (beads) were deployed on all four cores from which slurries were intended to be made at this site. For each slurry two subsamples were processed: (1) a sample of the slurry to

check contamination and (2) a scraping from the outer surface of the core to confirm deployment of beads.

Bead deployment was confirmed from the outer core scrapings in all four cores that were sampled for slurry preparation. No beads were detected in samples from the prepared slurries, indicating that they were probably free of contamination (data not shown).

Cultivations

Cultivations were normally conducted with slurries that were prepared by subcoring with 60-mL syringes from freshly broken whole-round core surfaces. Quantitative (most probable number [MPN]) and qualitative (enrichment) cultivations were started at temperatures between 4° and 80°C (Table T10). The media used were selective for fermenters, sulfate reducers, methanogens, and various anaerobic chemolithotrophic and heterotrophic prokaryotes that use iron(III) or manganese(IV) as an electron acceptor. Additionally, sulfite was added to some media. Sulfite can be used as an electron acceptor by sulfate-reducing bacteria or can be disproportionated to sulfide plus sulfate (suffix $–SO_3$ in Table T10). In order to determine the spore-forming portion of the community, some media were inoculated with pasteurized (10 min at 80°C) sediment (prefix past– in Table T10). Furthermore, some MPN assays were incubated under air (suffix $–O_2$ in Table T10)in order to enrich facultative or strict aerobic prokaryotes (see Table T10, p. 91, in the "Explanatory Notes" chapter).

T10. Media inoculated with material from Site 1231, p. 63.

Many recent and relict worm burrows were filled with what appeared to be iron sulfide and pyrite, indicating that sulfate reduction was occurring or had occurred (see "Unit I," p. 7, in "Description of Lithostratigraphic Units" in "Lithostratigraphy"). Therefore, samples from the burrows were used for enrichments of sulfate-reducing bacteria at 4° and 19°–21°C.

FISH-SIMS

^{13}C substrate incubations were initiated for postcruise analysis by FISH-SIMS using master slurry material from Cores 201-1231B-1H, 2H, 6H, and 12H. The ^{13}C substrates used were methane, acetate, and glucose. Glucose was used in Cores 201-1231B-1H and 2H. Acetate was used at all four depths, with multiple bottles at each depth. Additionally, incubations with methane were initiated with material from Cores 201-1231E-3H, 4H, and 5H.

PHYSICAL PROPERTIES

At Site 1231, three deep holes (Holes 1231B, 1231D, and 1231E; a maximum of 121.9 mbsf penetration) and two shallow holes (Holes 1231A and 1231C; <15.0 mbsf penetration) were cored. Physical property measurements in Hole 1231B involved standard-resolution multisensor track (MST), IR camera imaging, thermal conductivity, and discrete samples for moisture and density (MAD). Cores from the remaining four holes were run on the MST only. Additional thermal conductivity measurements were made on cores from Holes 1231D and 1231E to better define an important thermal property transition. High-resolution MST data were acquired on Hole 1231C.

Site 1231 has the same location as DSDP Leg 34, Site 321 (Shipboard Scientific Party, 1976). However, this is the first thorough physical property investigation of this site because of different cruise objectives and advances in instrumentation. At Site 1231 the entire sediment column was cored by APC, providing high-quality core for analysis.

Each section of whole-round core that was analyzed for physical properties was equilibrated to laboratory temperature (2–4 hr) and then run on the MST. The standard-resolution measurements were magnetic susceptibility (spacing = 5 cm, data acquisition scheme [DAQ] = 2 × 1 s), gamma ray attenuation (GRA) densitometer (spacing = 10 cm, count time = 5 s), *P*-wave velocity (spacing = 10 cm, DAQ = 10), and natural gamma radiation (NGR) (spacing = 30 cm, count time = 15 s). Thermal conductivity measurements were made on the third section of each whole round core in Hole 1231B, where possible, and in three sections from Hole 1231D. Some sections of Holes 1231B and 1231E were removed from the catwalk for microbiology and IW sampling. Physical properties were measured on these sections only if intact parts remained following the sampling. However, the intact record from Hole 1231D provides excellent continuity and spatial resolution of the physical property record.

MAD, *P*-wave velocity from the digital velocimeter, and resistance data (translated to formation factor as detailed in **"Formation Factor,"** p. 47, in "Physical Properties" in the "Explanatory Notes" chapter) were collected regularly only from Hole 1231B. MAD samples were taken at a frequency of one per section and at higher resolution in sections with lithologic transitions. MAD samples were co-located with the methane headspace extractions, where possible, to facilitate the volumetric analysis of methane concentrations.

Instrumentation, measurement principles, and data transformations are further discussed in **"Physical Properties,"** p. 41, in the "Explanatory Notes" chapter.

In general, the stratigraphic section at Site 1231 is characterized by several obvious lithologic changes that are clearly defined by the physical property data. Within individual lithologic zones, the physical property data are relatively constant. A major property change takes place at the Unit II/III boundary (55.4 mbsf) at the siliceous ooze/nannofossil ooze contact. A record of variable terrigenous input is superimposed on these two major biogenic intervals. Changes in the proportion of clay and volcanic glass within the biogenic facies produce distinct zones of physical property variation. Evidence of downhole compaction is weakly present in the resistivity and *P*-wave velocity data.

In the following sections, we describe the main characteristics of each physical property, relating it to the lithostratigraphic divisions given in **"Lithostratigraphy,"** p. 6.

Infrared Scanner

The IR scanner was employed on Hole 1231B cores to obtain data from a site where little temperature variation within individual cores was expected. The effects on core liner temperatures of variables such as wireline trip time and drill floor residence time will be investigated postcruise. Measurements of split-core surface temperature variation after equilibration to ambient laboratory temperature were made in order to study the relationship between lithology, water content, and emissivity. These data will be examined after the cruise.

Magnetic Susceptibility

Low-field volume magnetic susceptibility was measured on the MST using the Bartington loop sensor as described in "Magnetic Susceptibility," p. 44, in "MST Measurements" in "Physical Properties" in the "Explanatory Notes" chapter. Data were collected on WRC sections from Holes 1231A, 1231B, 1231D, and 1231E at standard resolution (spacing = 5 cm, count time = 1.0 s) (Fig. F8). Hole 1231C was run at high resolution (spacing = 1 cm, count time = 0.1 s). Data from all holes match well over the common intervals. A slight vertical offset in some cores on the order of 50 cm is not consistent downhole and is not significant to overall trends.

Unit I extends from 0 to 31 mbsf and is a diatomaceous ooze in which the clay proportion increases steadily from top to bottom. Magnetic susceptibility of the top 11 m varies around an average of ~25 × 10^{-5} SI units. Decreasing values in the top 1 mbsf may be due to reduction of iron, and this is supported by color changes over the same interval (see "Lithostratigraphy," p. 6). Between 11 and 20 mbsf, a zone of gray-green siliceous ooze containing some terrigenous material is characterized by low susceptibility (~5 × 10^{-5} SI units). The magnetic susceptibility boundary between the two is sharp, whereas the lithologic transition appears to be more gradual. At 20 mbsf a gradual increase in magnetic susceptibility commences coincident with increasing clay content of the sediments. Susceptibility stabilizes at 30 × 10^{-5} SI units at 24 mbsf and then increases only slightly to ~35 × 10^{-5} SI units. The Unit I/II boundary, located at 31 mbsf, corresponds to a drop from 35 × 10^{-5} to 20 × 10^{-5} SI units. Below this boundary values increase rapidly to 35 × 10^{-5} SI units and remain relatively stable to 45 mbsf.

The top of the dark brown clay (Subunit IIB) is at 45 mbsf, and the interval over which it is present, from 45–55 mbsf, comprises two magnetic subzones. From 45 to 51 mbsf, the susceptibility increases from ~35 × 10^{-5} to 50 × 10^{-5} SI units. At 51 mbsf, there is an abrupt increase to >100 × 10^{-5} SI units, which is maintained with minor variation to the base of Subunit IIB at 55 mbsf.

The Unit II/III boundary represents the contact between overlying clays and dense nannofossil ooze. The magnetic susceptibility across Subunit IIIA is characteristically and constantly low (~7 × 10^{-5} to 8 × 10^{-5} SI units). At the boundary between Subunits IIIA and IIIB (65 mbsf), the susceptibility abruptly increases to ~110 × 10^{-5} SI units, which is maintained to 68 mbsf. Between 68 and 70 mbsf, the signal drops back to ~15 × 10^{-5} SI units before returning to ~55 × 10^{-5} SI units across a narrow interval from 70 to 71mbsf. The peaks in this interval from 65 to 71 mbsf are caused by two dark brown terrigenous layers that are separated by nannofossil ooze.

At the top of Subunit IIIC, magnetic susceptibility falls abruptly to ~5 × 10^{-5} SI units and remains constant at this level until the base of the subunit at 107 mbsf.

Below 107 mbsf, the magnetic susceptibility gradually increases to a peak at 70 × 10^{-5} SI units at the bottom of the hole. The lithology at the base of the hole is an orange-brown nannofossil ooze. Its color indicates the presence of oxide minerals and suggests a chemical interaction with basaltic basement.

F8. Magnetic susceptibility data, p. 39.

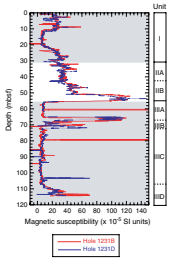

Paleomagnetism

At Site 1231 we collected 18 discrete samples for paleomagnetic measurements. The sampling frequency was one from each core in Cores 201-1231B-1H through 6H (0.0–50.9 mbsf) and two samples from each core below this interval to the bottom of the hole (Cores 201-1231B-7H through 12H; 50.9–112.3 mbsf). Alternating-field (AF) demagnetization of the natural remanent magnetization (NRM) was conducted up to 40 mT in 10- or 5-mT steps. Anhysteretic remanent magnetization (ARM) was measured to 40 mT in 10-mT steps with a 29-µT direct current–biasing field. AF demagnetization of the ARM was conducted to 40 mT in 10-mT steps.

Hole 1231B shows high magnetic intensity except in Cores 201-1231B-2H through 3H (Fig. F9). In the uppermost sample (201-1231B-1H-3, 14–16 cm), we were able to isolate a stable magnetic direction after 25-mT AF demagnetization, overcoming the drilling-induced overprint (Fig. F10). Cores 201-1231B-4H through 8H show abnormal demagnetization behavior. Volcanic glass–rich clay layers are present within this interval of lithostratigraphic Unit II (see "Description of Lithostratigraphic Units," p. 7, in "Lithostratigraphy") and these show high NRM intensities and high intensities after 40-mT AF demagnetization (Fig. F9). Intensity decreases at 5-to 30-mT AF demagnetization, then intensity increases at 35- to 40-mT AF demagnetization (Figs. F11).

Nannofossil ooze samples from lithostratigraphic Subunit IIIC (see "Description of Lithostratigraphic Units," p. 7, in "Lithostratigraphy") have a high magnetic intensity despite low susceptibility (Fig. F9). All samples from this interval have a downward inclination, which corroborates the result of Ade-Hall and Johnson (1976). Pale orange-yellow semiopaque, mineral-bearing nannofossil ooze of Unit III (Sample 201-1231B-9H-1, 50–52 cm) shows a more stable magnetization (Fig. F12).

Density and Porosity

Density data were measured on the MST by the GRA densitometer (spacing = 10 cm, count time = 5 s) and were calculated from split-core mass/volume measurements. Porosity was calculated from the split-core samples. Average bulk density values from the two MST runs and the discrete samples show good agreement across the entire downhole section (Fig. F13). A major exception was located across Subunit IIIA (55–66 mbsf), where the two MST runs differ by ~15% (average = 2.15 g/cm³ for Hole 1231B and 1.85 g/cm³ for Hole 1231D). The data from this interval in Hole 1231B are unrealistically high and inconsistent with all other measurements. Therefore, those data points have been eliminated from the figure. The only operational problem at this time was sticking of the MST boat because of a dirty track, but this does not explain the extent of the error. There are a number of other localized exceptions (e.g., 29–31, 47–50, 89–93, and 98–100 mbsf) where the two MST data sets differ. Overall, these do not detract from a description of the general trends, but the values cited for Hole 1231B should be treated with caution.

The top 11 m of Unit I exhibits a slightly curved density profile. Density is 1.2 g/cm³ at 0 mbsf, rises to 1.25 g/cm³ at 5 mbsf, and declines to 1.2 g/cm³ at 11 mbsf. From 11 to 20 mbsf (the zone of green siliceous ooze), density is steady, varying slightly around 1.2 g/cm³. From 20 to

F9. Magnetic intensity and susceptibility, p. 40.

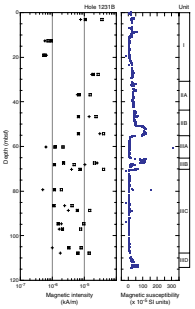

F10. Principal component analysis, 201-1231B-1H-3, 14–16 cm, p. 41.

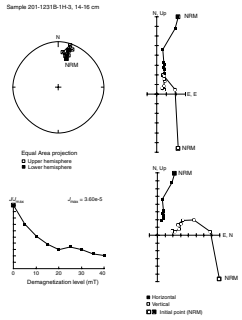

F11. Principal component analysis, 201-1231B-4H-4, 80–82 cm, p. 42.

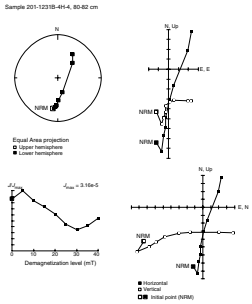

F12. Principal component analysis, 201-1231B-10H-7, 28–30 cm, p. 43.

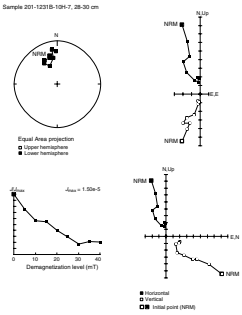

50 mbsf density is slightly more variable, ranging between 1.2 and 1.3 g/cm³. There is not a pronounced density change at the Unit I/II boundary. At 50 and 55 mbsf, there are two steplike increases in density to a high of 1.8 g/cm³ at 55.5 mbsf. This density increase clearly highlights the Unit II/III boundary.

Porosity varies between 85% and 90% from 0 to 45 mbsf. There are five noticeable lows at 3, 12, 30, 38, and 45 mbsf, where the values are ~85% or lower. These are coincident with grain density lows but are not apparent in the bulk density data set. From 45 to 55 mbsf (Subunit IIB), the porosity gradually decreases to 80%. In this interval, a large decrease in the grain density is coincident with a zone of high clay and volcanic glass content and secondary zeolite mineralization. At 55.5 mbsf, the Unit II/III boundary is again clearly marked by a drop in porosity to 55%. The grain density increases to 2.75 g/cm³.

Unit III is a nannofossil ooze. Average bulk density across the whole unit is ~1.7–1.8 g/cm³. Grain density is around 2.75 g/cm³ and porosity remains low, at 58%–59%. These general trends are interrupted by two terrigenous layers at 65–68 and 69–70 mbsf. The terrigenous layers have lower bulk density (~1.5 g/cm³), higher grain density (~2.9 g/cm³), and higher porosity (up to 73%) than the dominant nannofossil ooze of the unit. The top and base of the terrigenous unit, at 66 and 71 mbsf, respectively, coincide with the boundaries of Subunits IIIA/IIIB and IIIB/IIIC. From 107 mbsf to the bottom of Subunit IIID at 114 mbsf, bulk density decreases to 1.65 g/cm³, grain density increases to 2.85 g/cm³, and porosity increases to 70%. It is possible that these trends are linked to chemical interaction with basaltic basement.

F13. Density and porosity data, p. 44.

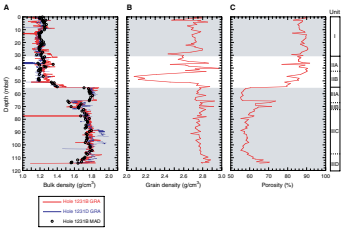

Compressional Wave Velocity

P-wave data from the MST *P*-wave logger (PWL) were recorded at a 10-cm spacing for all available APC cores from Holes 1231A, 1231B, 1231D, and 1231E and at 2-cm spacing for Hole 1231C. The PWS3 velocimeter was used to measure *P*-wave velocities on split cores from Hole 1231B, with measurements taken at least once per section (Fig. **F14A**). More closely spaced measurements were made at lithologic boundaries and at intervals marked by possible diagenetic modifications. The PWL-derived velocities are consistently 40–60 m/s slower than the PWS-derived velocities. This offset is consistent with that found at other sites and probably results from core liners incompletely filled with sediment. All velocities in this section are discussed in terms of PWS3 data.

The velocities increase slightly from 1520 to 1550 m/s from 0 to 50 mbsf (Unit I and Subunit IIA). In the dark brown terrigenous layer from 50 to 55 mbsf (Subunit IIB), velocities decrease steadily to a low of 1510 m/s. This decrease coincides with increasing bulk density and decreasing porosity (Fig. **F13**).

The abrupt sedimentological transition at the Unit II/III interface is apparent in the abrupt *P*-wave velocity increase to 1530 m/s at the boundary. Between 55 and 64 mbsf *P*-wave velocity drops to 1480 m/s. At 64 mbsf, *P*-wave velocities increase from 1480 to 1560 m/s over a 2-m interval. At the Subunit IIIA/IIIB boundary *P*-wave velocity drops back to ~1500 m/s across 1 m. The underlying dark brown terrigenous sediment of Subunit IIIB is characterized by velocity variations between 1510 and 1540 m/s. Velocities in the upper 20 m of Subunit IIIC trend upward, from 1540 to 1560 m/s, coincident with a bulk density increase

F14. *P*-wave velocity profiles, p. 45.

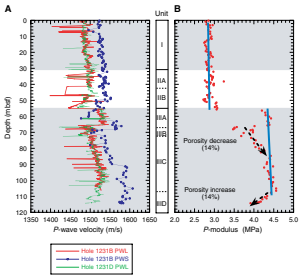

and a porosity decrease. A sudden velocity increase at 90 mbsf (to ~1590 m/s) is followed by a consistent but variable velocity of ~1580 m/s to the base of Subunit IIID. The 20-m/s oscillation around this trend appears to be related to porosity variation.

At first inspection, the sequence of velocity changes and the overall velocity increase from 1520 to ~1600 m/s could be indicative of mechanical compaction. We cannot constrain the actual in situ mechanical state, however, without consolidation testing or wireline velocity/density information. The following analysis examines the shipboard measurements in an attempt to isolate relict signatures of burial and/or diagenesis. To isolate the effects of density and porosity variation, we utilize the compressional wave modulus (*P*-modulus) transform, a combination of the effects of shipboard *P*-wave velocity and density profiles, as a proxy for mechanical state:

$$P\text{-modulus (MPa)} = V_p^2 \times \rho_{bw},$$

where,

V_p = *P*-wave velocity (km/s) and
ρ_{bw} = (wet) bulk density (g/cm³).

The plot of the *P*-modulus transform (Fig. **F14B**) shows a constant mechanical state (~2.8 Mpa) with small variations (±0.1 MPa), reflecting minor porosity oscillation in Units I and II. The steplike transition at the Unit II/III boundary is clearly reflected in *P*-modulus increase (from 2.8 to 4.4 MPa) and encompasses the intrinsic sediment fabric difference (most notably, the porosity drop of 22%) between the siliceous ooze and nannofossil ooze compositions. The ~0.1-MPa *P*-modulus increase to the top of Subunit IIID (108 mbsf) probably indicates a small relict burial compaction signature. The arrow-highlighted transitions (Fig. **F14B**) are porosity controlled and show the sensitivity of the depressurized, dominantly nannofossil sediment fabric state to non-nannofossil content (decreasing opaque or semiopaque minerals over 65–84 mbsf, with the reverse trend over 108–114 mbsf).

Natural Gamma Ray Emission

NGR was measured on the MST for all Site 1231 holes (spacing = 30 cm, count time = 15 s), except for Hole 1231C, which was run at a higher spatial resolution (spacing = 15 cm, count time = 30 s). The data are plotted in Figure **F15** as uncorrected average counts per second (cps).

F15. NGR profiles, p. 46.

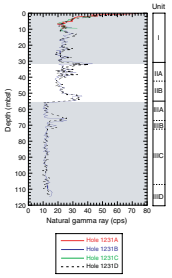

NGR is relatively high at the seafloor (~70 cps), but declines rapidly over the first 6 mbsf to the Unit I/II average of ~22 cps. This transition may reflect redox-related uranium enrichment resulting from high organic content (see **"Natural Gamma Ray Emission,"** p. 31, in "Physical Properties" in the "Site 1226" chapter). At this time, shipboard organic carbon data are not available to test this hypothesis. The NGR baseline of ~22 cps is consistent to near the base of Unit II. Increased emission intervals at the top of Subunit IIA and the bottom of Subunit IIB coincide with minima in grain density transitions that mark maximum terrigenous content. The combination of low porosity and grain density with high gamma radiation, particularly in Subunit IIB, suggests that these narrow zones are clay-rich concentrations.

At the Unit II/III boundary, natural gamma radiation drops to 10–12 cps, except for the clay-rich interval (up to 22 cps) that comprises Subunit IIIB. The increased NGR of Subunit IIIB is consistent with the clay enrichment signature in Unit II. The stable NGR signal over Subunit IIID further strengthens the supposition that changing color and apparent consolidation result from diagenetic processes rather than a change in clay content.

Formation Factor

Formation factor (longitudinal and transverse) was determined for Hole 1231B as described in "Formation Factor," p. 47, in "Physical Properties" in the "Explanatory Notes" chapter with a minimum sample interval of one per section. All formation factor data were co-located (within 3 cm) with discrete (PWS3) *P*-wave velocity measurements. As expected (except in Subunit IB), formation factor data (Fig. F16) show inverse proportionality to porosity (i.e., Archie's Law). Consistent with the *P*-wave velocity analysis, formation factor data exhibit no indication of significant consolidation.

Longitudinal formation factors range between 1.7 and 2.15 in the clayey siliceous oozes of Unit I, with a decreasing trend that reflects a small porosity increase over the interval of ~2–27 mbsf (Fig. F13). Over Unit II, formation factors range between 1.6 and 3.1, with oscillations about the indicated trend lines (Fig. F16). These oscillations represent porosity variation of ±2%–5% about the interval trend (88%–85% for Subunit IIA and 85%–80% for Subunit IIB). The counterintuitive formation factor decrease in Subunit IIB probably reflects a gradational change in pore structure that corresponds to a rapidly increasing clay mineral and metal oxide content (see "Lithostratigraphy," p. 6). The abrupt lithologic change at the Subunit IIB/Unit III boundary results in a sharp increase in formation factor that is correlated with a porosity reduction from 80% to 57%. Below the *Discoaster* interval (55.3–65 mbsf), formation factors range between 2.8 and 3.9, with the variation controlled by porosity. The final ~0.3 m above basement shows a large increase in formation factor, jumping from ~3.2 to 6.8. Such a rapid change probably indicates a significant increase in diagenetic deposition in pore throats, given the minor total porosity decrease from 70% to 65% and small bulk density increase (Fig. F13).

F16. Formation factor profile, p. 47.

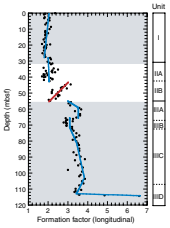

Thermal Conductivity

Thermal conductivity measurements were made in Hole 1231B at a rate of one per core (usually the third section, at 75 cm, if this was available). In order to better resolve the conductivity change associated with the lithologic transition at the Unit II/III boundary, additional measurements were made in Holes 1231D and 1231E (Fig. F17A). Values range between 0.70 and 1.26 W/(m·K) (average = 0.95 W/[m·K]). The abrupt transition between the siliceous sediments to nannofossil ooze is clear in the thermal conductivity increase (from ~0.73 to ~1.20 W/[m·K]) between 54.5 and 55.3 mbsf. Within the two lithology-differentiated intervals (Units I/II and Unit III, respectively), thermal conductivity changes are controlled by water content (Fig. F17B).

F17. Thermal conductivity, p. 48.

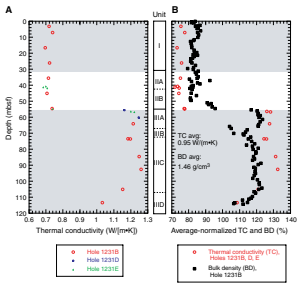

Summary and Discussion

At Site 1231 the direct relationship between physical properties and lithologic variation is more obvious than at any other site during the leg. The principal sedimentary types overlying basaltic basement are a nannofossil ooze overlain by a siliceous ooze, with the boundary (Unit II/III interface) at 55 mbsf. The nannofossil ooze is characterized by low magnetic susceptibility, very low gamma radiation, and high bulk density. The high bulk density is related to a markedly lower porosity in the nannofossil unit compared with the siliceous ooze. We suggest this difference is a result of the dissimilarity between the constituent microfossils making up the two units. Small flattened nannofossil plates allow a much tighter initial packing and lower porosity than the larger open diatom frustules. The only significant evidence for burial compaction or diagenesis occurs in the basal 0.3 m of the sedimentary section. There is little grain density variation across the entire cored section, reflecting the small density difference between dominantly quartz/silica above and calcite below.

Above 55 mbsf (Units I and II) the sedimentary section is characterized by higher gamma radiation and magnetic susceptibility signatures and lower bulk density and *P*-wave velocity. The gamma radiation increase is probably a result of variable clay content in the sequence. The base of the clays in the sediment sequence is at 70 mbsf, with the peak of input between 55 and 50 mbsf. Above this level, clay content gradually declines but is still present up to the seafloor.

Of note in the sequence is the sharp-bounded magnetic susceptibility low between 11 and 20 mbsf. This zone lies within an otherwise gradationally changing lithologic sequence. This suggests the anomalously low magnetic signature here is not of primary depositional origin.

DOWNHOLE TOOLS

At Site 1231, the downhole tools employed were the Adara temperature shoe and the DVTP-P. The results of the temperature and pressure measurements at Site 1231 are described in the two sections below.

In Situ Temperature Measurements

Six downhole temperature determinations were made at Site 1231 using three Adara tool deployments in Hole 1231B, two in Hole 1231D, and one in Hole 1231E. An Adara temperature shoe deployment at the seafloor yielded a value for the bottom-water temperature of 1.75°C. Table **T11** summarizes all of the Site 1231 temperature measurements.

The combined downhole temperature profile exhibits a noticeable change in gradient somewhere between 41.4 and 60.4 mbsf. A relatively steep gradient in the upper part of the sediment column of 0.090°C/m changes to a more moderate gradient of 0.035°C/m in the lower part (Fig. **F18A**). Using the lower gradient, the extrapolated temperature at the sediment/basement interface is 8.6°C. Figure **F18B** shows the temperature data with two theoretical steady-state conductive temperature profiles calculated using a seafloor temperature of 1.75°C and the measured thermal conductivities from the Hole 1231B cores. Like the temperature data, the simulated profiles show a marked gradient change at 55 mbsf because of a marked change in sediment composition and corresponding large increase in thermal conductivity from ~0.7 W/(m·K)

T11. Downhole temperatures, p. 64.

F18. Temperature vs. depth, p. 49.

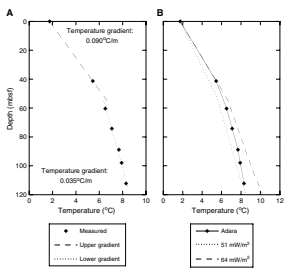

above this depth to ~1.2 W/(m·K) below (Fig. F18). The two simulated profiles bracket the data, but it is not possible to fit both the upper and lower gradients with a steady-state conductive model using the measured conductivities. Other hypotheses to explain the temperature data such as fluid flow and basement temperature variations should be explored. The two conductive profiles provide a range for the heat flow of 51–64 mW/m².

Davis-Villinger Temperature-Pressure Probe

The DVTP-P was deployed once at Site 1231 at a depth of 107.9 mbsf (after Core 201-1231A-12H). The results of this deployment may indicate minor overpressure in the formation relative to the base of the hole (Fig. F19). The expected 0.7-MPa spike was present at the start of the deployment, but the pressure dropped rapidly within a minute and then stabilized at a flat value for the rest of the 30-min run. The recorded value for the formation is 0.02 MPa higher than that recorded in the base of the hole at the end of the run. Assuming that the tool was raised ~1 m for the stop at the base of the hole, the formation may be slightly overpressured. The data quality suffers from heave during the deployment (average > 2 m). For a reasonable formation permeability of ~10^{-16} m², the measured overpressure would be adequate to produce flow at a rate of ~0.4 mm/yr. On the basis of chloride data, upward flow at this site is estimated to be ~2 mm/yr (see "Biogeochemistry," p. 12)

F19. DVTP-P pressure, p. 50.

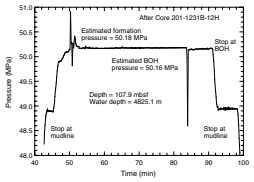

REFERENCES

Ade-Hall, J.M., and Johnson, H.P., 1976. Paleomagnetism of sediments, Leg 34. *In* Yeats, R.S., Hart, S.R., et al., *Init. Repts., DSDP,* 34: Washington (U.S. Govt. Printing Office) 533–539.

Berggren, W.A., Kent, D.V., Swisher, C.C., and Aubry, M.P., 1995. A revised Cenozoic geochronology and chronostratigraphy. *In* Berggren, Kent, Aubry, and Hardenbol, J., (Eds.), *Geochronology, Time Scales and Global Stratigraphic Correlation*. Spec. Pub.—SEPM 59:129–212.

Blechschmidt, G., 1976. Biostratigraphy of calcareous nannofossils: Leg 34, Deep Sea Drilling Project. *In* Yeats, R.S., Hart, S.R., et al., *Init. Repts. DSDP,* 34: Washington (U.S. Govt. Printing Office), 705–712.

Boström, K., Joensuu, O., Valdés, S., Charm, W., and Glaccum, R., 1976. Geochemistry and origin of East Pacific sediments sampled during DSDP Leg 34. *In* Yeats, R.S., Hart, S.R., et al., *Init. Repts. DSDP,* 34: Washington (U.S. Govt. Printing Office), 556–574.

Brady, S., and Gieskes, J.M., 1976. Interstitial water studies, Leg 34. *In* Yeats, R.S., Hart, S.R., et al., *Init. Repts., DSDP,* 34: Washington (U.S. Govt. Printing Office), 625–628.

Bunch, T.E., and LaBorde, R., 1976. Mineralogy and compositions of selected basalts from DSDP Leg 34. *In* Yeats, R.S., Hart, S.R., et al., *Init. Repts., DSDP,* 34: Washington (U.S. Govt. Printing Office), 263–275.

Dymond, J., Corliss, J.B., and Stillinger, R., 1976. Chemical composition and metal accumulation rates of metalliferous sediments from Sites 319, 320, and 321. *In* Yeats, R.S., Hart, S.R., et al., *Init. Repts. DSDP,* 34: Washington (U.S. Govt. Printing Office), 575–588.

Parkes, R.J., Cragg, B.A., Bale, S.J., Getliff, J.M., Goodman, K., Rochelle, P.A., Fry, J.C., Weightman, A.J., and Harvey, S.M., 1994. A deep bacterial biosphere in Pacific Ocean sediments. *Nature,* 371:410–413.

Shipboard Scientific Party, 1976. Site 321. *In* Yeats, R.S., Hart, S.R., et al., *Init. Repts., DSDP,* 34: Washington (U.S. Govt. Printing Office), 111–153.

Smith, D.C., Spivack, A.J., Fisk, M.R., Haveman, S.A., Staudigel, H., and ODP Leg 185 Shipboard Scientific Party, 2000. Methods for quantifying potential microbial contamination during deep ocean coring. *ODP Tech. Note,* 28 [Online]. Available from the World Wide Web: <http://www-odp.tamu.edu/publications/tnotes/tn28/INDEX.HTM>. [2002-03-30]

Yeats, R.S., Hart, S.R., et al., 1976. *Init. Repts., DSDP,* 34: Washington (U.S. Govt. Printing Office).

Figure F1. Lithostratigraphic summary for Site 1231. TD = total depth.

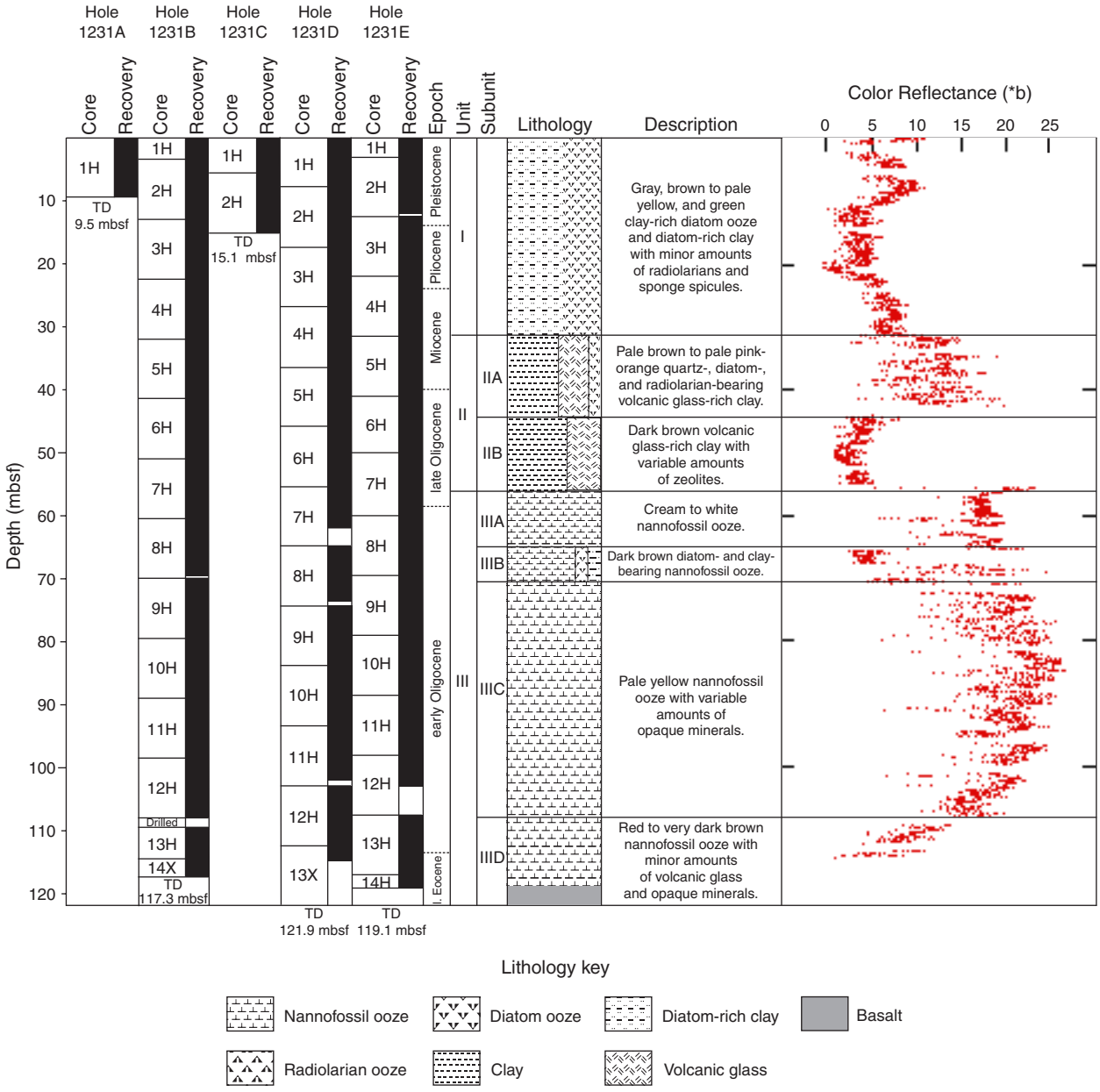

Figure F2. Close-up photographs. **A, B.** Redox boundary between red (above 64 cm) and gray clay-rich diatom ooze containing a large black sulfide nodule at 100–104 cm in Unit I. (Continued on next two pages.)

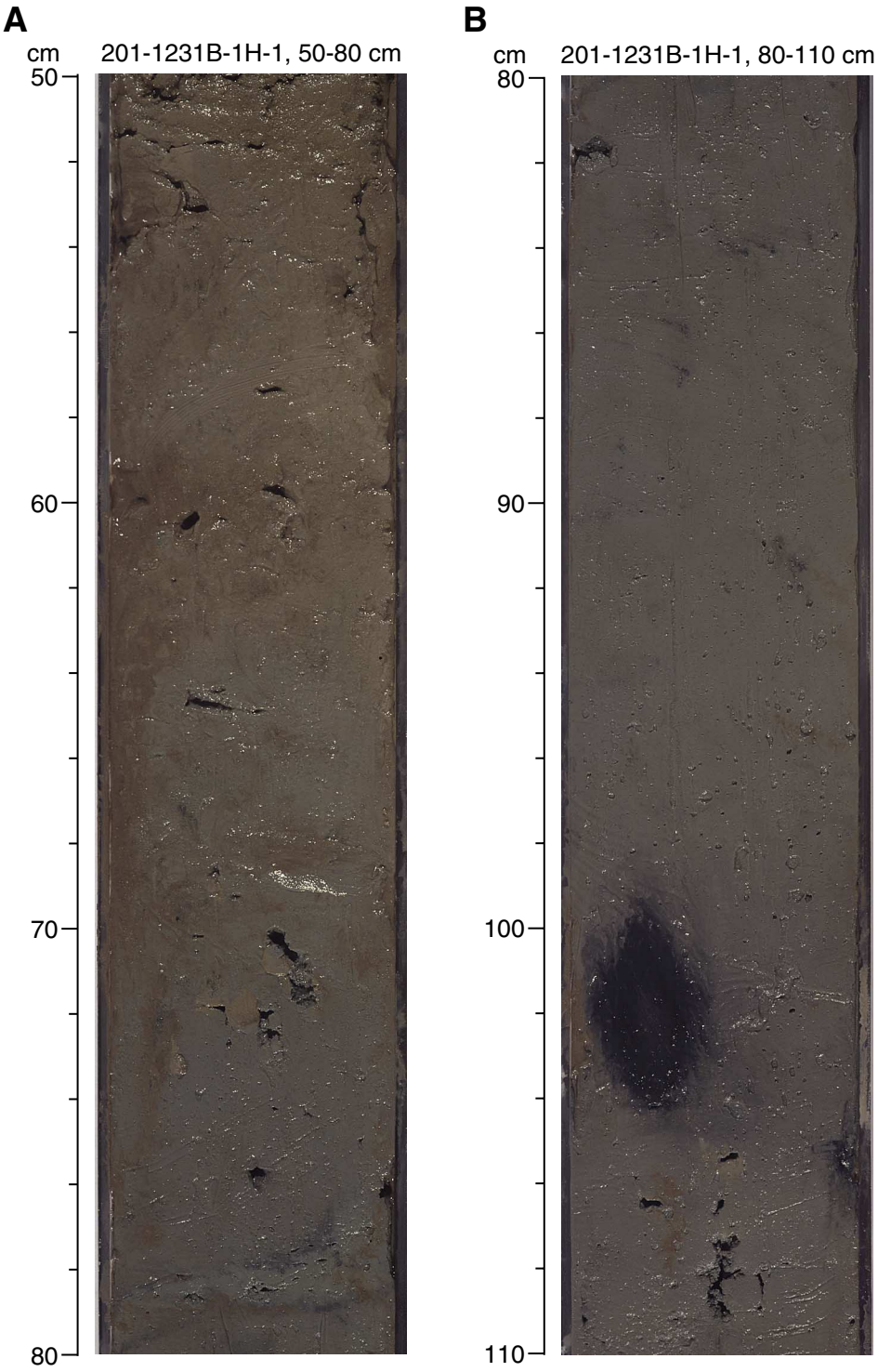

Figure F2 (continued). **C.** Color change from gray to green clay-rich diatom ooze in Unit I. Note the dark sulfide-rich layer present at the boundary (~35 cm). **D.** Trace fossils in orange clay sediments of Subunit IIA. (Continued on next page.)

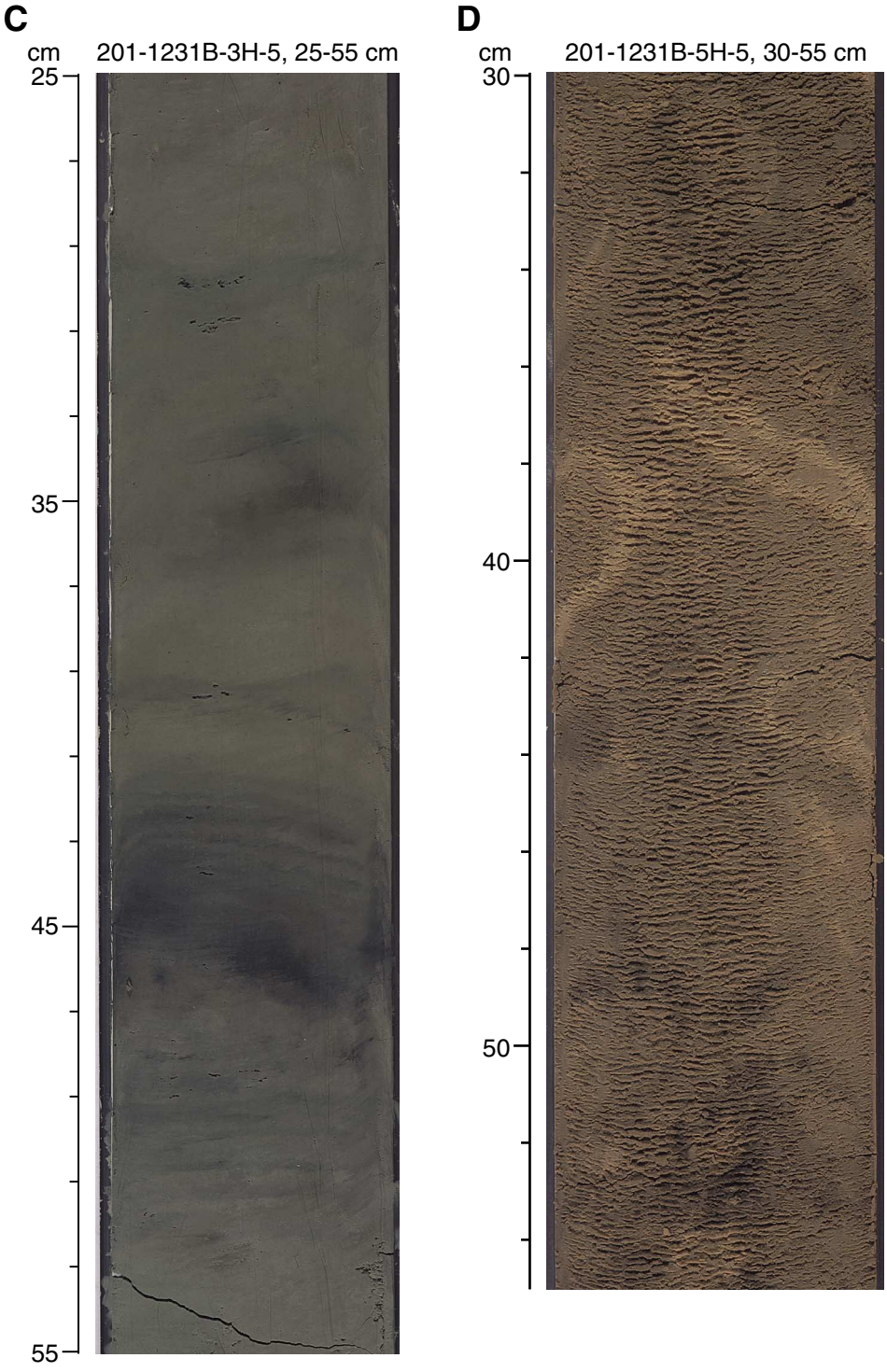

Figure F2 (continued). E. Sharp boundary (at 73 cm) between white nannofossil ooze of Subunit IIIA and brown nannofossil ooze of Subunit IIIB. Note the large sulfide nodule present at ~77 cm, right below the boundary.

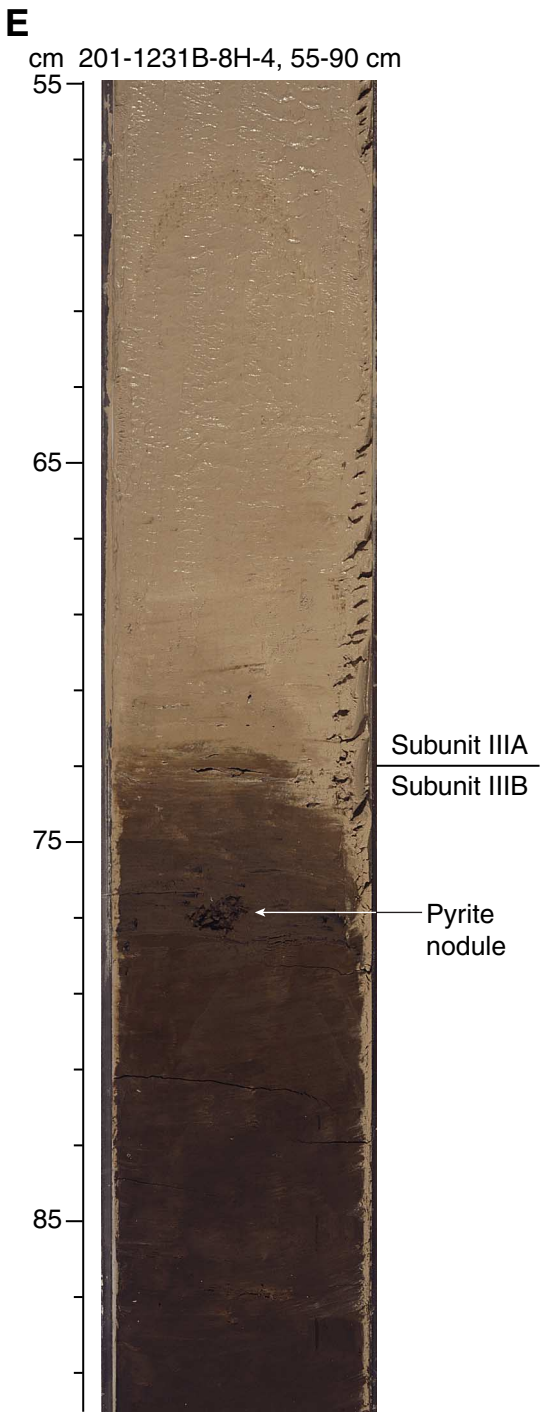

Figure F3. Concentrations of various dissolved species in interstitial waters from Holes 1231B and 1231E. (**A**) Alkalinity, (**B**) dissolved inorganic carbon (DIC), (**C**) nitrate, (**D**) manganese, (**E**) iron, (**F**) sulfate, and (**G**) strontium. (Continued on next two pages.)

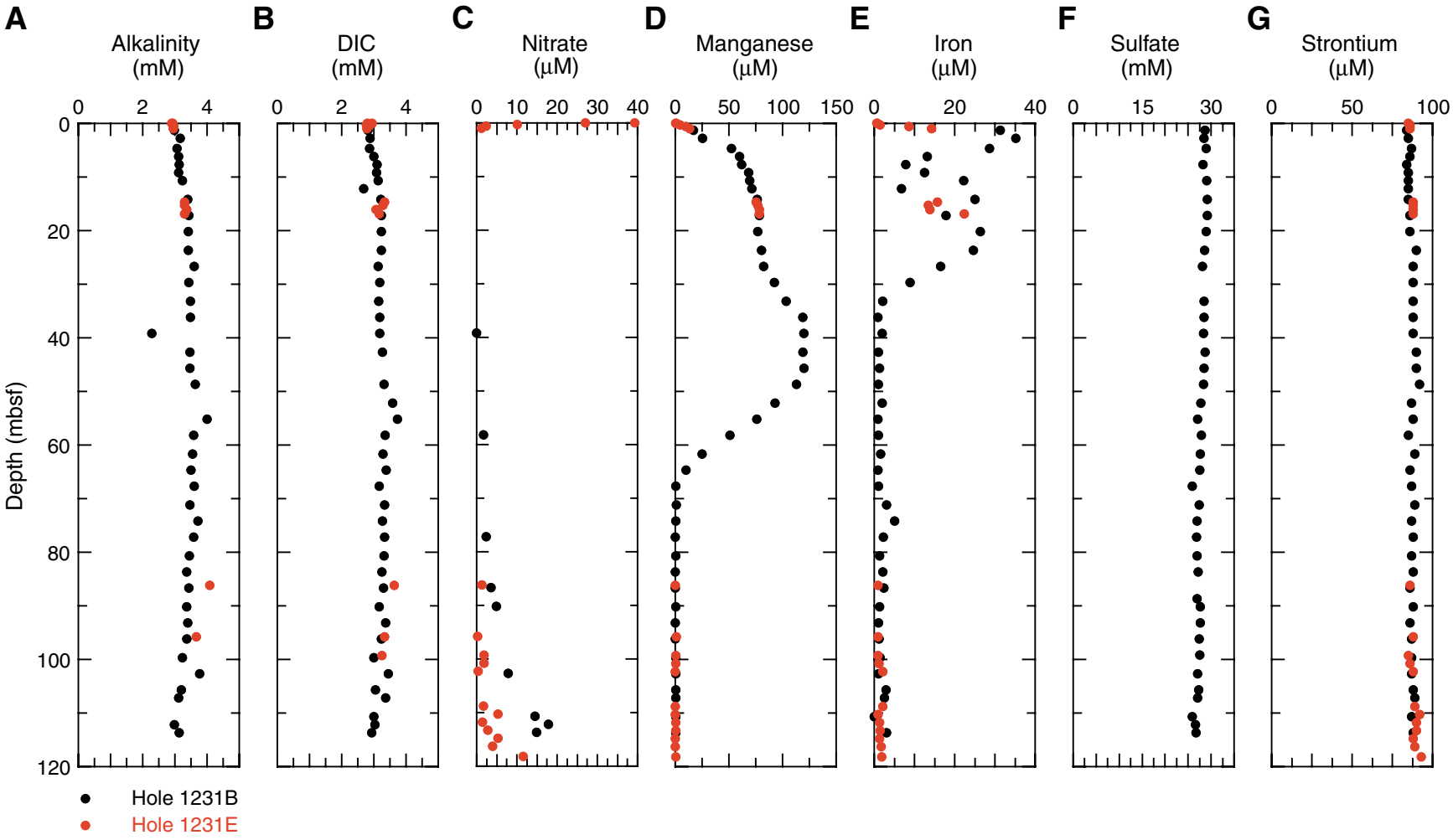

Figure F3 (continued). (**H**) lithium, (**I**) barium, (**J**) total sulfide, (**K**) acetate, (**L**) formate, (**M**) hydrogen, and (**N**) methane. (Continued on next page.)

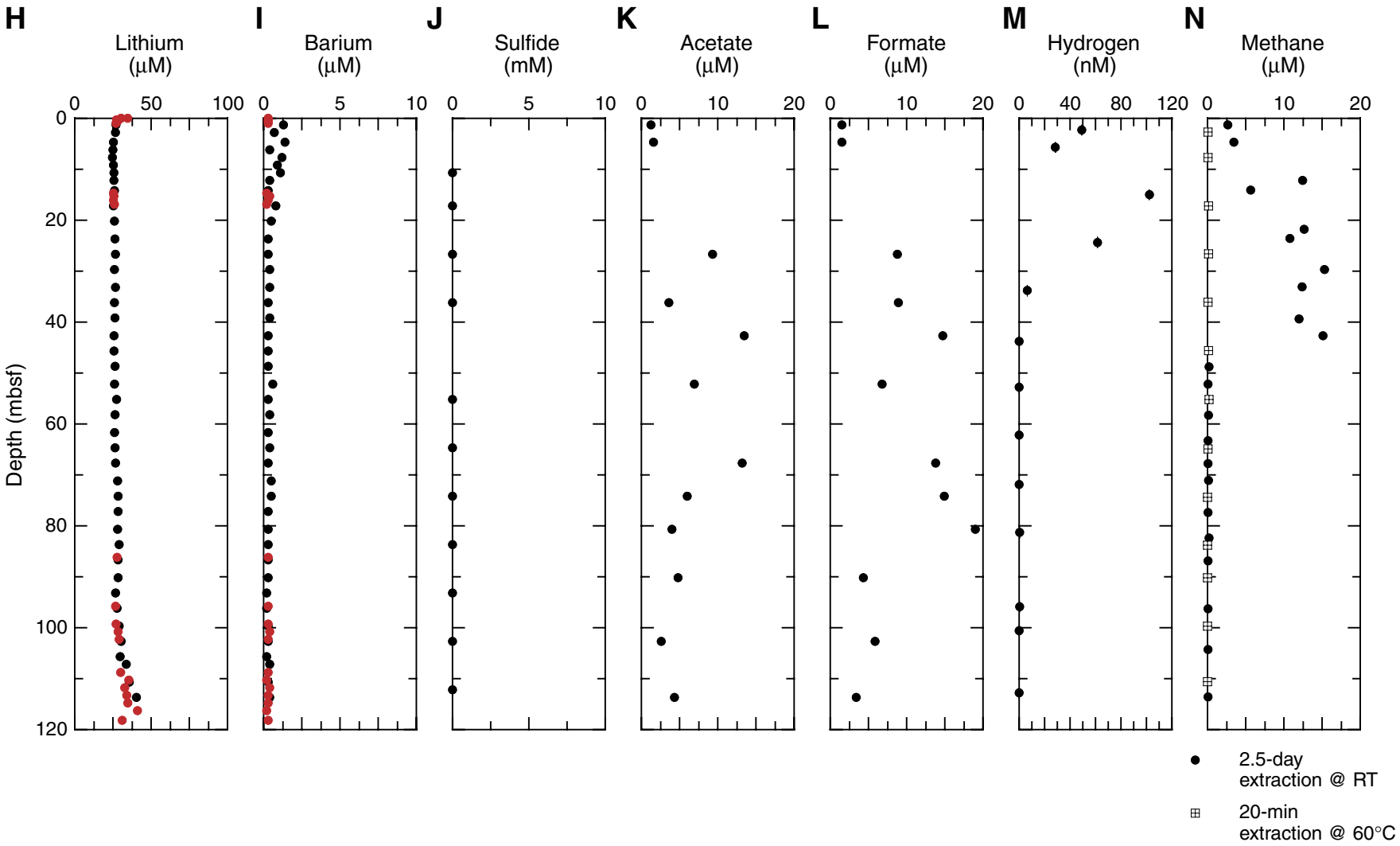

Figure F3 (continued). (O) ammonium, (P) phosphate, (Q) silica, and (R) chloride.

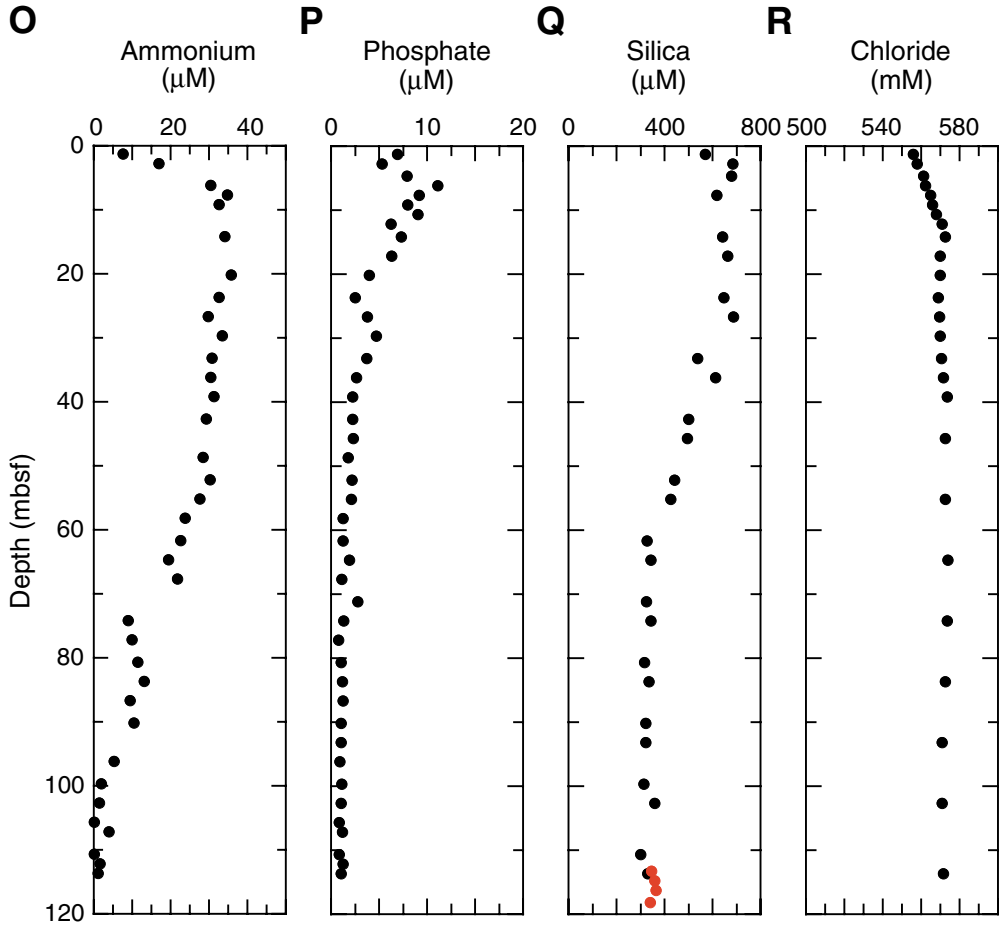

Figure F4. Subsampling and analysis program for the MBIO core sections from Hole 1231B. The sequence of subsections runs from the top of the core (right) to the bottom (left). DNA = deoxyribonucleic acid, ATP = adenosine triphosphate. WRC = whole-round core. See Table T2, p. 82, in the "Explanatory Notes" chapter for explanation of sampling codes.

Hole 1231B		Activity measurements: methanogenesis, thymidine incorporation, tritiated hydrogen turnover, ^{18}O phosphate turnover					Sulfate reduction activity; hydrogen concentration; CH4/C2H6 concentrations; magnetic bacterial particles				Biomarkers	Diffusion experiments	Cell separations	Fe/Mn/S solid-phase concentrations and stable isotopes	Sulfate Reduction Pressure-Temperature experiments	General enrichment slurry						Fluorescent in situ hybridization (FISH)	DNA						DNA-ODP archive	ATP-DNA	------Top of Section------
		N_2-flushed cutting rig									ODP cutter																					
Interval (cm)			6		6		6				10	5	5	5	5	6				7	7	5	5	5	5	5	5	5	5	10	
Curators Code		H3S	ABTP	O-18B	ABTP	PO4B	SRRF	H2S	CNSS	CHNSF	BIOMHIN	DIFFF	CELLS	FESF	SRRWF	SLURH	SLURJ	SLURB	LDC	SLUR		FISHWR2	FISHWR	DNAM	DNAI	DNAT	DNAN	DNAS	DNAODP	ATPS	
Sample Type		2 Syr	4 Syr	1 Syr	8 Syr	1-cm slice	4 Syr	4 Syr	1-cm slice	1-cm slice	WRC	WRC	WRC	WRC	WRC	2 x 5-mL syr	1 x 5-mL syr	2 x 5-mL syr	1 x 5-mL syr	60-mL syr	60-mL syr	WRC	WRC	WRC	WRC	WRC	WRC	WRC	WRC	WRC	
Package Type		Al-bag	Anaer. Jar	Al-bag	Anaer. Jar	Poly-bag	Al-Bag	Poly-bag	Poly-bag	Al-bag	Poly-bag	Al-bag	Poly-bag	Al-bag	Al-bag	Al-bag	Al-bag	Anaer. Jar	Al-bag	Slurry flask	Slurry flask	Al-bag	Poly-bag	Poly-bag	Poly-bag	Poly-bag	Poly-bag	Poly-bag	Poly-bag	Poly-bag	
Package Atmosphere		N_2	N_2	N_2	N_2		N_2	N_2		Vac pack		Vac pack		Vac pack	N_2+ Ancult	N_2	N_2	N_2	N_2	N_2	N_2	N_2									
Temperature Destination		+4˚C Radvan	+4˚C Radvan	+4˚C Radvan	+4˚C Radvan	-20˚C	+4˚C Radvan	+4˚C	+4˚C	+4˚C	-80˚C	+4˚C	-80˚C	-20˚C	+4˚C	+4˚C	+4˚C	+4˚C	+4˚C	on ice	on ice	+4˚C	-80˚C	-80˚C	-80˚C	-80˚C	-80˚C	-80˚C	-80˚C	-80˚C	Sediment Depth (mbsf)
Core	Section																														top
1H	1	-	-	-	-	-	-	-	-	-	-	1	-	1	-	-	-	-	-	-	-	1	-	-	1	-	-	-	-	-	0.0
1H	2	1	1	1	1	1	1	1	1	1	1	-	-	1	1	1	1*	1	1	1	1	1	1	-	1	1	1	1	1	1	1.5
2H	2	1	1	1	1	1	1	1	1	1	1	-	-	1	-	1	-	1	1	1	1	1	1	1	1	1	1	1	1	1	4.9
2H	5	-	-	-	-	-	-	-	-	-	-	-	-	1	-	-	-	-	-	-	-	-	-	-	-	-	-	-	-	-	9.4
3H	2	1	1	1	1	1	1	1	1	1	1	-	-	1	1	-	-	-	-	-	-	1	1	-	1	1	1	1	1	1	14.4
3H	5	-	-	-	-	-	-	-	-	-	-	1	-	1	-	-	-	-	-	-	-	-	-	-	-	-	-	-	-	-	18.9
4H	2	1	1	1	1	1	1	1	1	1	1	-	-	1	-	-	-	-	-	-	-		-		1	1	1	1	1	1	23.9
4H	5	-	-	-	-	-	-	-	-	-	-	-	-	1	-	-	-	-	-	-	-	-	-	-	-	-	-	-	-	-	28.4
5H	2	1	1	1	1	1	1	1	1	1	1	-	-	1	-	-	-	-	-	-	-	-	-		1	1	1	1	1	1	33.4
5H	5	-	-	-	-	-	-	-	-	-	-	-	-	1	-	-	-	-	-	-	-	-	-	-	-	-	-	-	-	-	37.9
6H	2	1	1	1	1	1	1	1	1	1	1	-	-	1	1	1	-	1	1	1	1	1	1	1	1	1	1	2	1	1	42.9
6H	5	-	-	-	-	-	-	-	-	-	-	-	-	1	-	-	-	-	-	-	-	-	-	-	1	1	1	1	1	1	47.4
7H	2	1	1	1	1	1	1	1	1	1	1	-	-	-	-	-	-	-	-	-	-	-	-		1	1	1	1	1	1	52.4
7H	5	-	-	-	-	-	-	-	-	-	-	1	-	1	-	-	-	-	-	-	-	-	-	-	1	1	-	1	-	-	56.9
8H	2	1	1	1	1	-	1	1	-	-	1	-	-	1	-	-	-	-	-	-	-		-		1	1	1	1	1	1	61.9
8H	5	-	-	-	-	-	-	-	-	-	-	-	-	1	-	-	-	-	-	-	-	-	-	-	-	-	-	-	-	-	66.4
9H	2	1	1	1	1	1	1	1	1	1	1	-	-	1	1	-	-	-	-	-	-	1	1		1	1	1	1	1	1	71.4
9H	5	-	-	-	-	-	-	-	-	-	-	-	-	1	-	-	-	-	-	-	-	-	-	-	-	-	-	-	-	-	75.9
10H	2	1	1	1	1	1	1	1	1	1	1	-	-	1	-	-	-	-	-	-	-				1	1	1	1	1	1	80.9
10H	5	-	-	-	-	-	-	-	-	-	-	-	-	1	-	-	-	-	-	-	-	-	-	-	-	-	-	-	-	-	85.4
11H	2	-	-	-	-	-	-	-	-	-	-	-	-	1	-	-	-	-	-	-	-		-	-	-	-	-	-	-	-	90.4
11H	5	1	1	1	1	1	1	1	1	1	1	-	-	1	1	-	-	-	-	-	-	-	-	-	1	1	1	1	1	1	94.9
12H	2	1	1	1	1	1	1	1	1	1	1	-	1	1	-	1	-	1	1	1	1	1	1		1	1	1	1	1	1	99.9
12H	5	-	-	-	-	-	-	-	-	-	-	-	-	1	-	-	-	-	-	-	-	-	-	-	-	-	-	-	-	-	104.4
13H	3	1	1	1	1	1	1	1	1	1	1	-	-	1	1	-	-	-	-	-	-	-	-		1	1	1	1	1	1	112.4
	TOTAL	13	13	13	13	12	13	13	12	12	13	3	1	24	6	4	1	4	4	4	4	7	6	2	16	15	14	16	14	14	

Figure F5. Subsampling and analysis program for the MBIO core sections from Hole 1231E. The sequence of subsectioning runs from the top of the core (right) to the bottom (left). DNA = deoxyribonucleic acid, WRC = whole-round core. See Table T2, p. 82, in the "Explanatory Notes" chapter for explanation of sampling codes.

Hole 1231E				Biomarkers	Sulfate Reduction Pressure-Temperature experments	Enrichments for Mn(IV) reducers		Fluorescent in situ hybridization (FISH)		DNA			DNA-ODP archive	-----Top of Section ------
		ODP cutter												
Interval (cm)		5	5	10	5	5	5	5	5	5	5	5	5	
Curators Code		H3S	H2S	BIOMHIN	SRRWF	MnIV Reducer		FISHWR2	FISHWR	DNAI	DNAT	DNAS	DNAODP	
Sample Type		WRC	WRC	WRC	WRC	WRC	WRC	WRC	WRC	WRC	WRC	WRC	WRC	
Package Type		Al-bag	Al-bag	Poly-bag	Al-bag	Al-bag	Al-bag	Al-bag	Poly-bag	Poly-bag	Poly-bag	Poly-bag	Poly-bag	
Package Atmosphere		N_2	N_2		N_2+ Ancult	N_2	N_2	N_2						
Storage Temperature		+4˚C Radvan	+4˚C	-80˚C	+4˚C	+4˚C	+4˚C	+4˚C	-80°C	-80˚C	-80˚C	-80˚C	-80˚C	Sediment Depth (mbsf)
Core	Section													top
1H	2	-	-	-	-	1	1	-	-	-	-	-	-	1.5
2H	5	1	1	1	-	1	1	1	-	1	1	1	1	8.9
3H	5	1	1	1	1	1	1	1	1	1	1	1	1	18.5
4H	5	1	1	1	-	1	1	1	1	1	1	1	1	28.0
5H	2	-	-	-	1	-	-	-	-	-	-	-	-	33.0
5H	5	-	-	1	-	1	1	2	1	1	1	1	1	37.5
6H	2	-	-	-	-	1	1	-	-	2	2	2	1	42.5
6H	5	-	-	1	1			-	-	1	1	1	1	47.0
7H	4	1	1	2	-	2	2	1	1	2	2	2	1	55.0
8H	4	-	-	2	-	2	2	-	-	2	2	2	2	64.5
9H	2	-	-	-	1	-	-	1	1	1	-	-	-	71.0
9H	5	-	-	-	-	-	1	-	-	-	-	-	-	75.5
11H	1	1	1	1	1	-	1	-	-	1	1	1	1	88.5
11H	6	-	-	-	-	-	1	-	-	-	-	-	-	96.0
12H	3	-	-	-	-	-	1	-	-	-	-	-	-	101.0
13H	5	-	-	-	-	-	1	-	-	-	-	-	-	113.5
14H	3	-	-	-	-	-	1	-	-	1	1	1	1	118.4
	TOTAL	5	5	10	5	10	16	7	5	14	13	13	11	

Figure F6. Total prokaryotic cells (solid circles) and the percentage of those cell numbers involved in cell division (open circles) with depth at Site 1231. Both total cell counts and dividing cell percentages become increasingly unreliable as total cell counts decrease below 4×10^6 cells/cm^3 as within-sample variability rises due to the low number of cells counted. Vertical dashed line on the left represents the significance limit at 4×10^5 cells/cm^3.

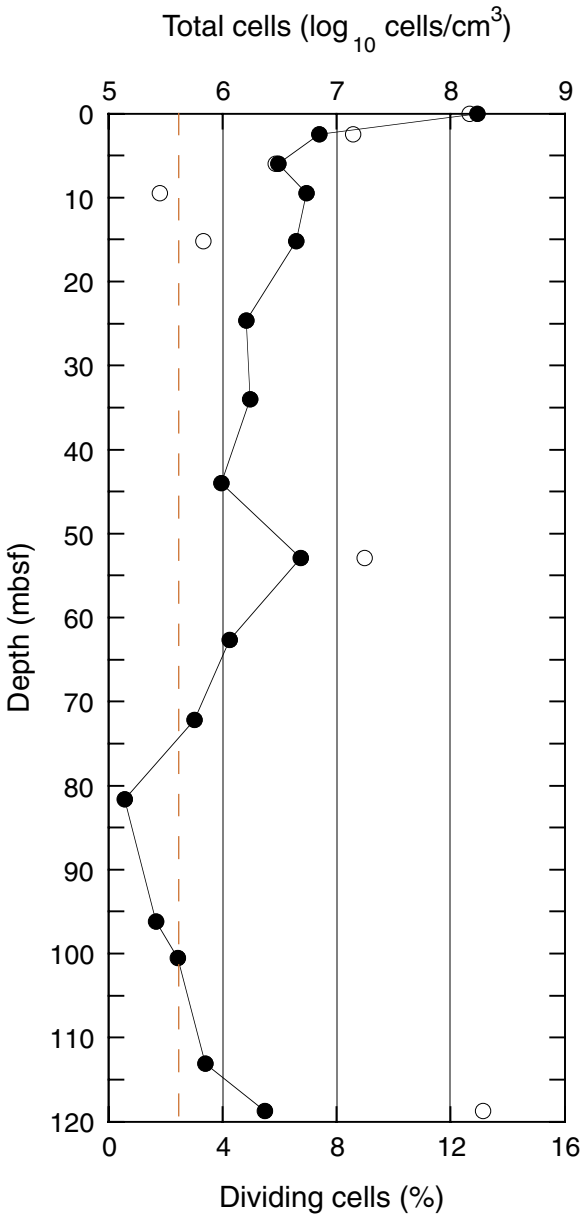

Figure F7. Profile of total prokaryotic cells at Site 1231. Heavy dashed line is a regression line derived from previous ODP legs and updated from Parkes et al., 1994 ($\log_{10}$ cells = 8.03 – 0.66 $\log_{10}$ depth), lighter dashed lines are the ±2-σ envelopes of cell concentrations from previously censused ODP sites.

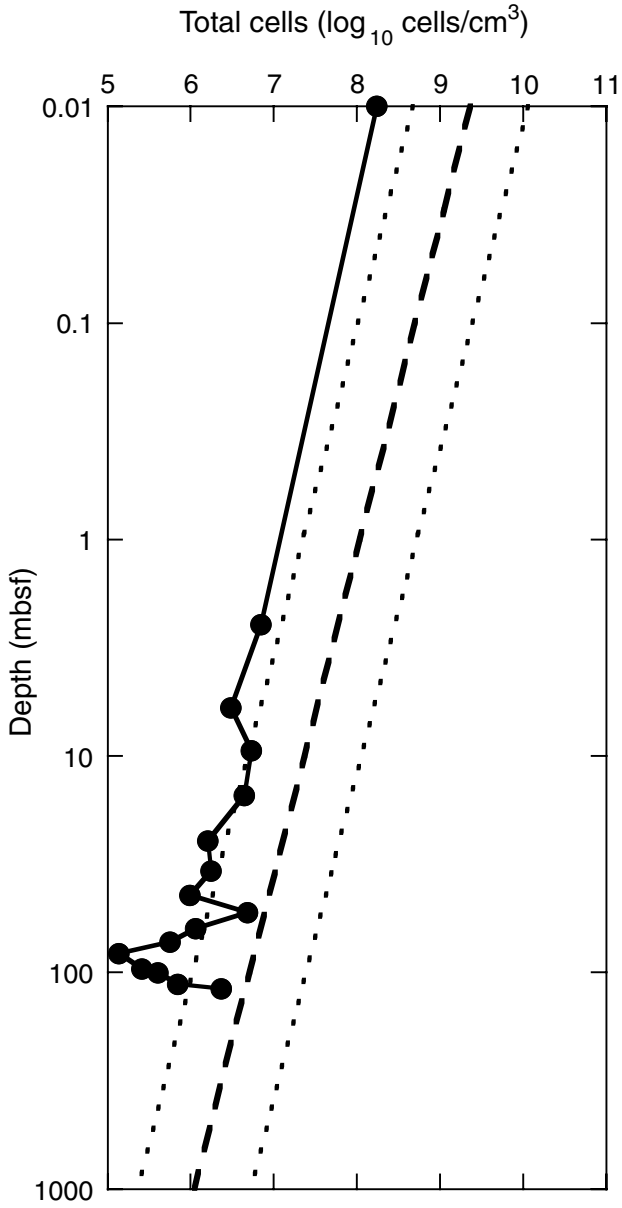

Figure F8. Magnetic susceptibility data from Holes 1231B and 1231D. Shaded areas in all figures are provided for differentiation of the lithostratigraphic units.

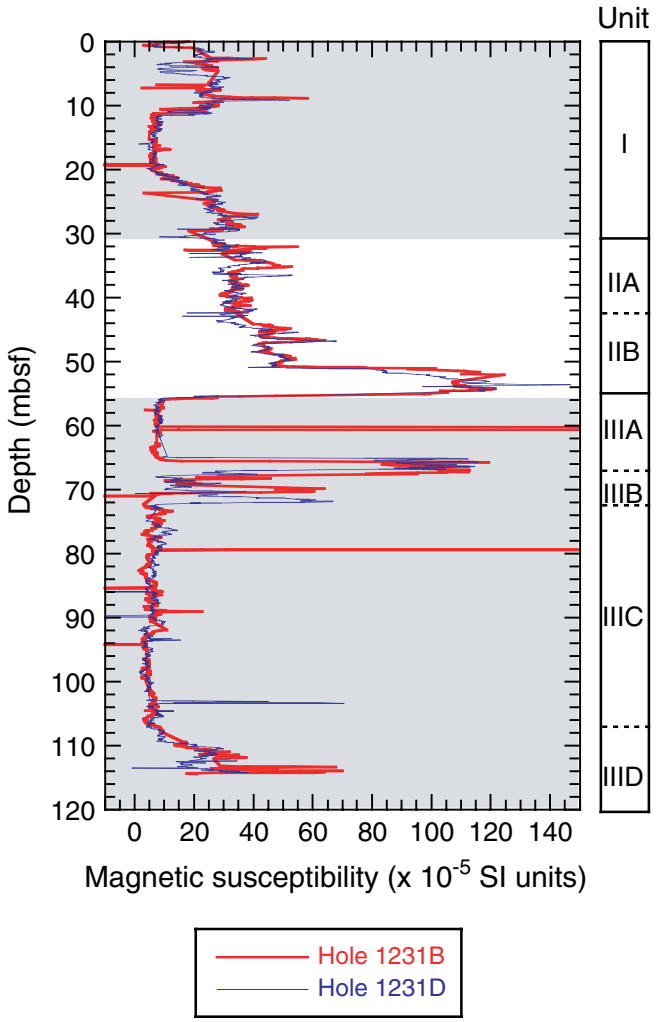

Figure F9. Magnetic intensity and susceptibility in Hole 1231B. Magnetic intensity shows NRM (open squares), 20-mT AF demagnetization (solid squares), and 40-mT AF demagnetization (crosses).

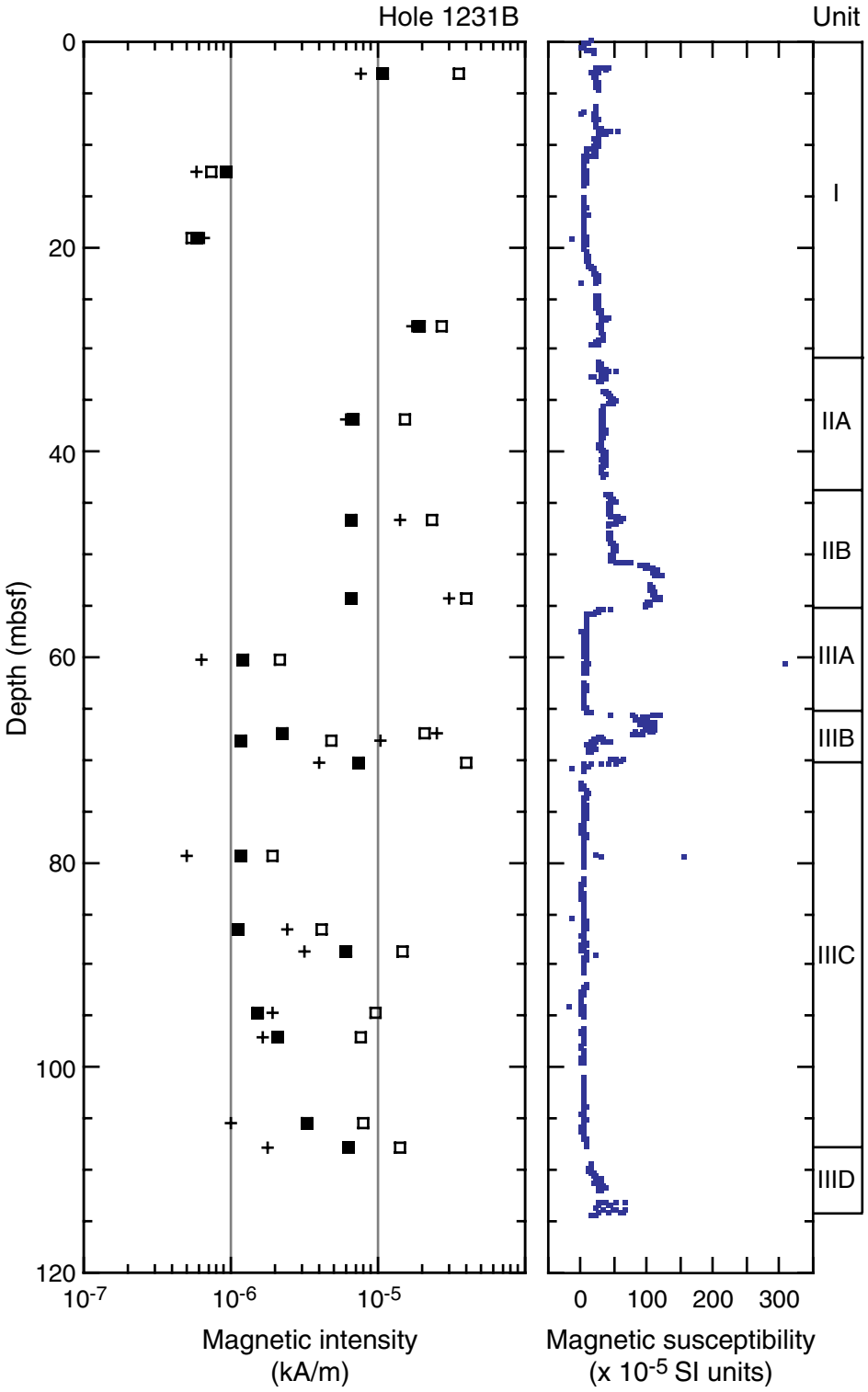

Figure F10. Principal component analysis of natural remanent magnetization (NRM) of Sample 201-1231B-1H-3, 14–16 cm, including equal area projection of directions of magnetization during demagnetization, intensity of magnetization plotted vs. demagnetization, and vector component diagrams showing projection of magnetic vector's endpoints on horizontal and vertical planes.

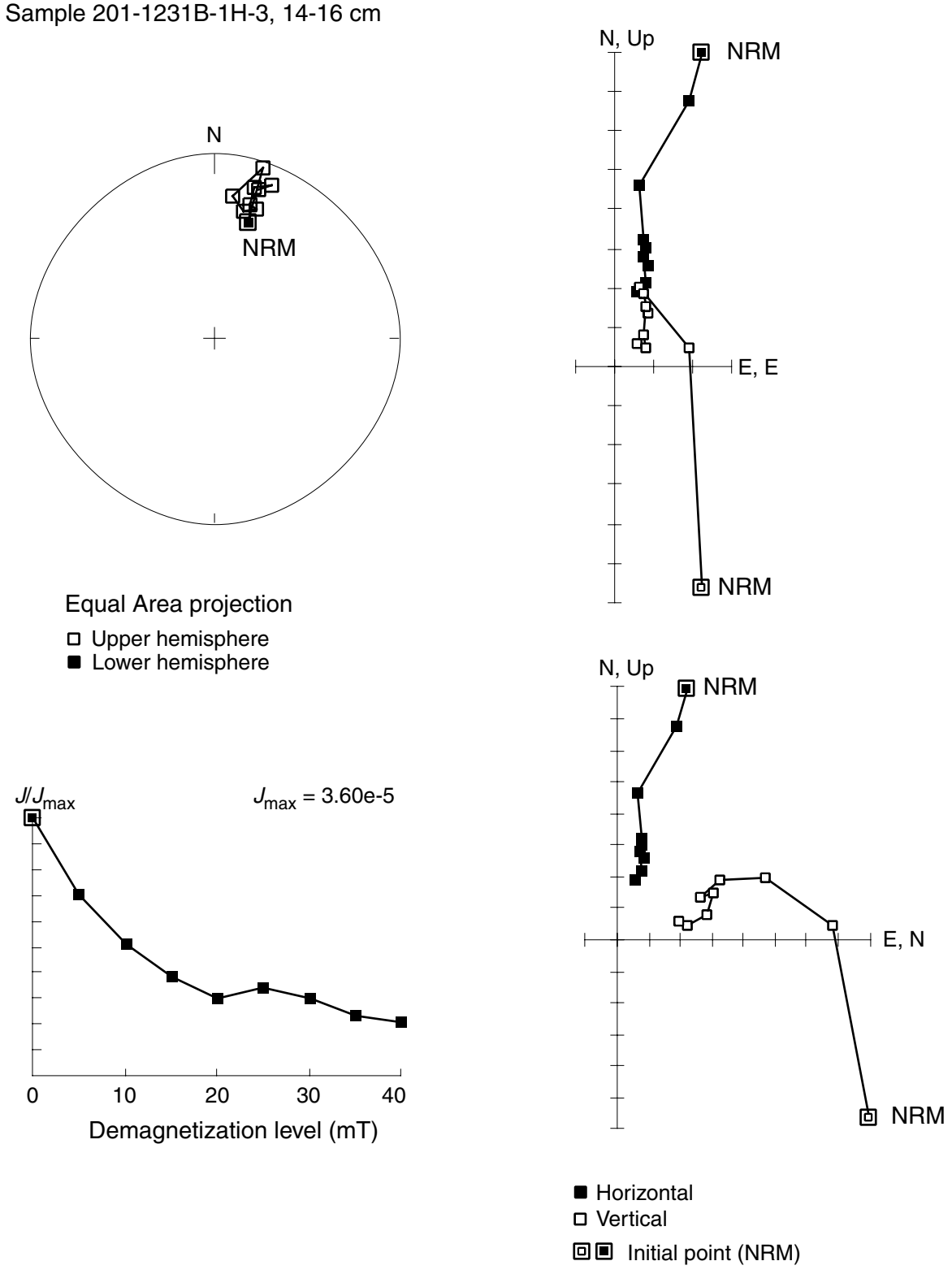

Figure F11. Principal component analysis of natural remanent magnetization (NRM) of Sample 201-1231B-4H-4, 80–82 cm, including equal area projection of directions of magnetization during demagnetization, intensity of magnetization plotted vs. demagnetization, and vector component diagrams showing projection of magnetic vector's endpoints on horizontal and vertical planes.

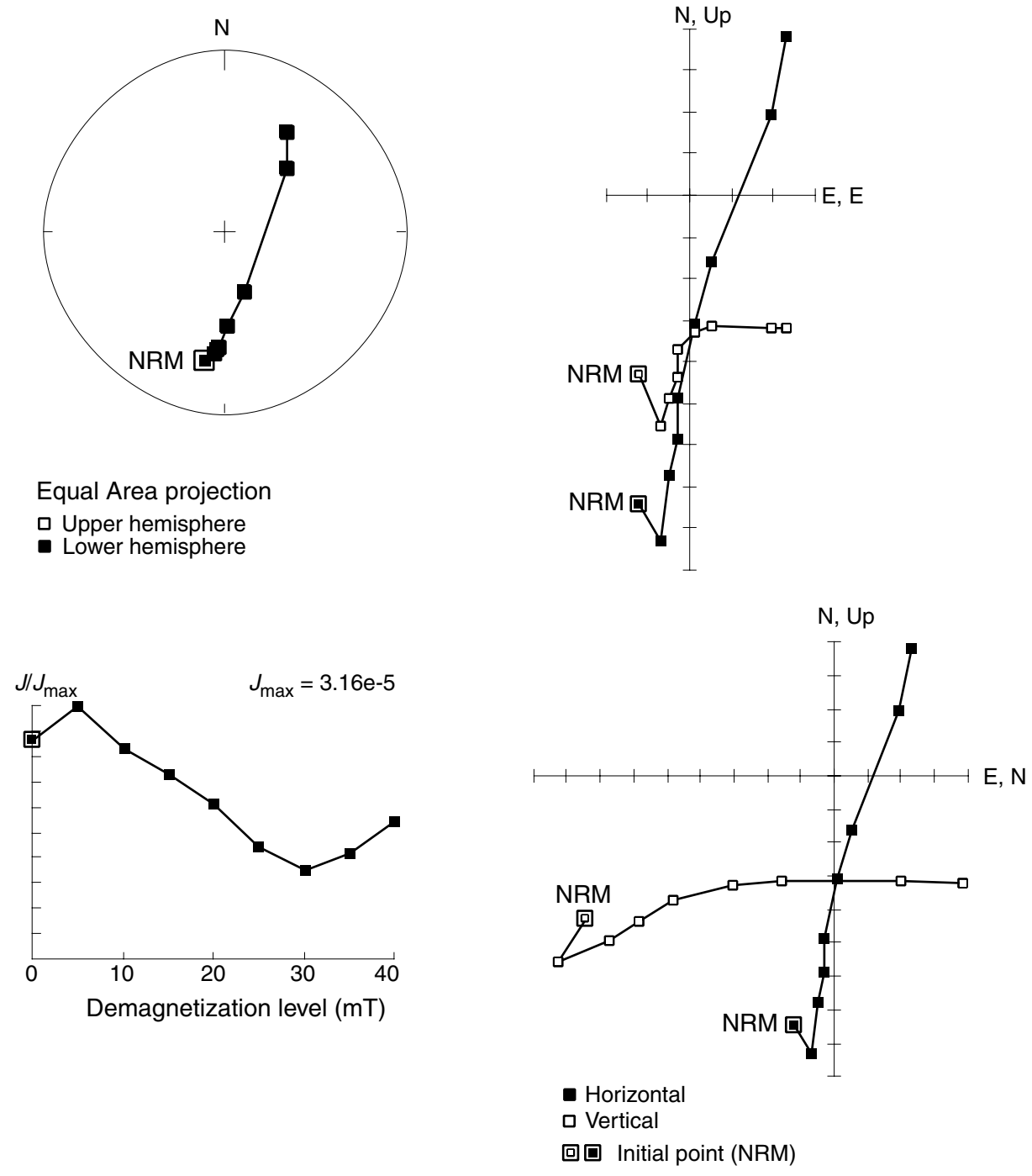

Figure F12. Principal component analysis of natural remanent magnetization (NRM) of Sample 201-1231B-10H-7, 28–30 cm including equal area projection of directions of magnetization during demagnetization, intensity of magnetization plotted vs. demagnetization, and vector component diagrams showing projection of magnetic vector's endpoints on horizontal and vertical planes.

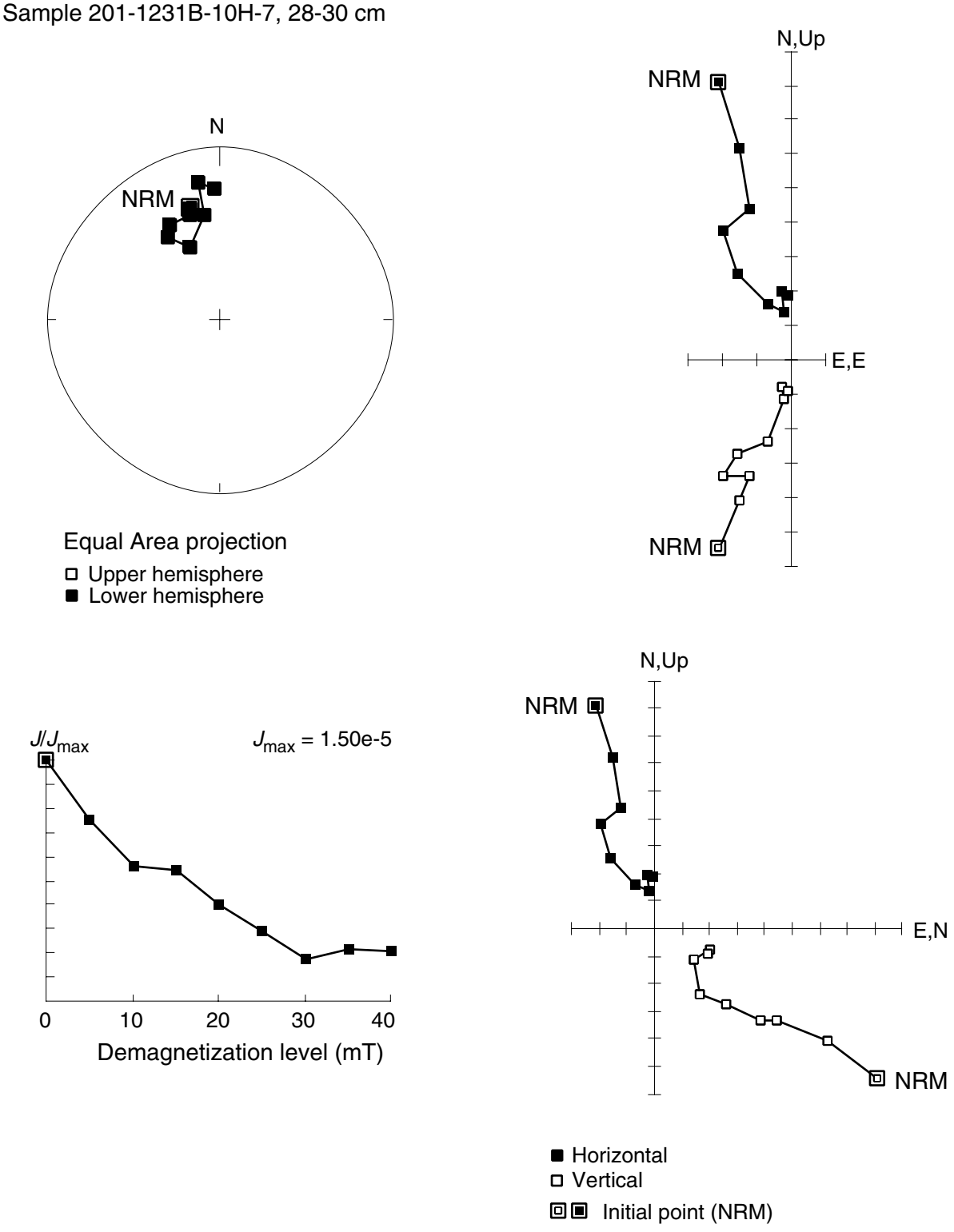

Figure F13. A. Gamma ray attenuation (GRA) and moisture and density (MAD) bulk density. **B.** Grain density (Hole 1231B). **C.** Porosity (Hole 1231B).

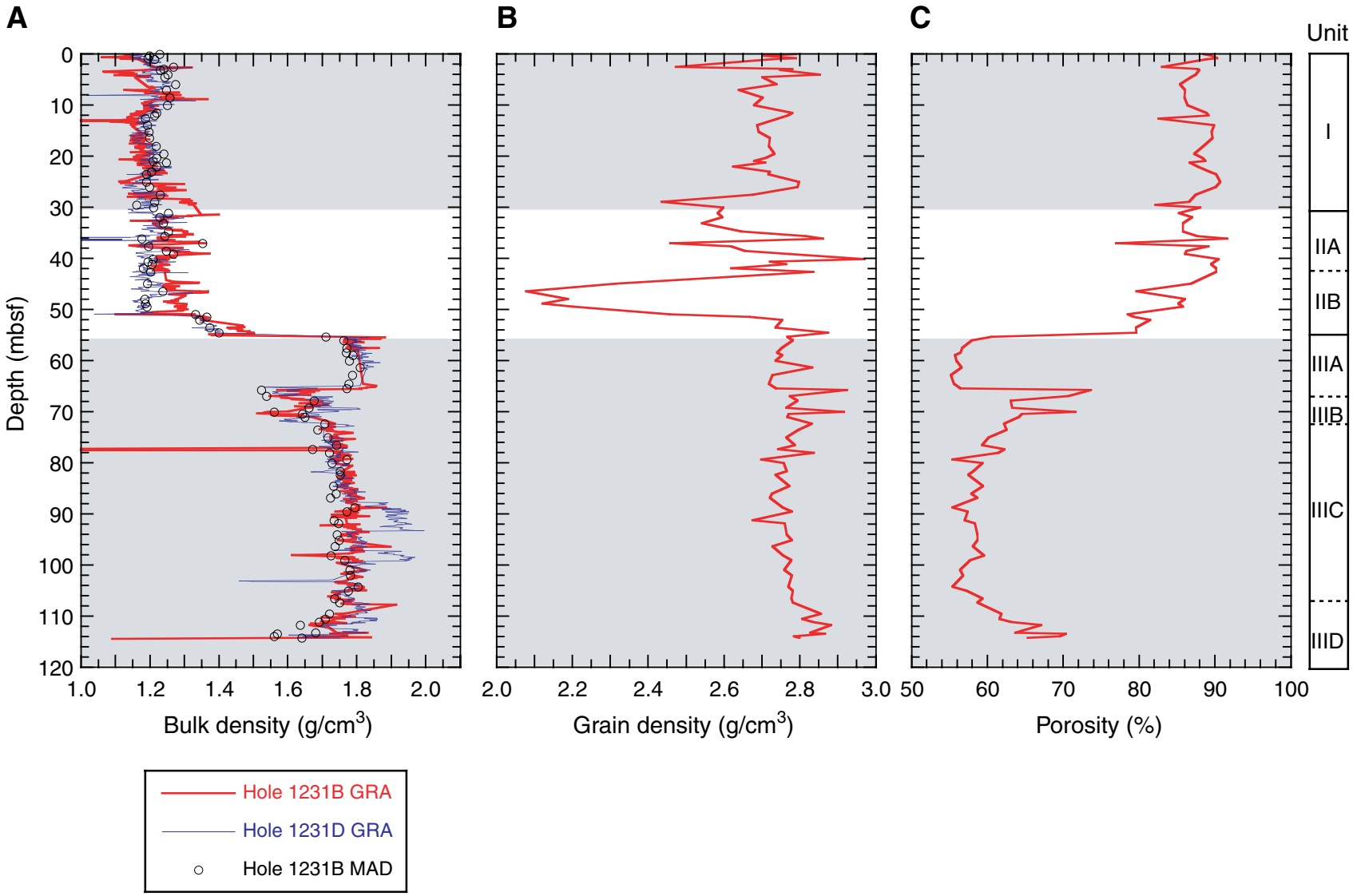

Figure F14. A. *P*-wave velocity profiles derived from *P*-wave logger (PWL) and Hamilton Frame contact probe (PWS3) measurements. **B.** *P*-modulus ($V_P^2 \times \rho_{bw}$) illustrates that sediment fabric and associated porosity variations control the different elastic behavior in Units I–II (siliceous ooze) and Unit III (nannofossil ooze), respectively. No burial-related compaction or diagenetic alteration is apparent in Units I–II, with a very small *P*-modulus increase in Unit III potentially representing a consolidation signature.

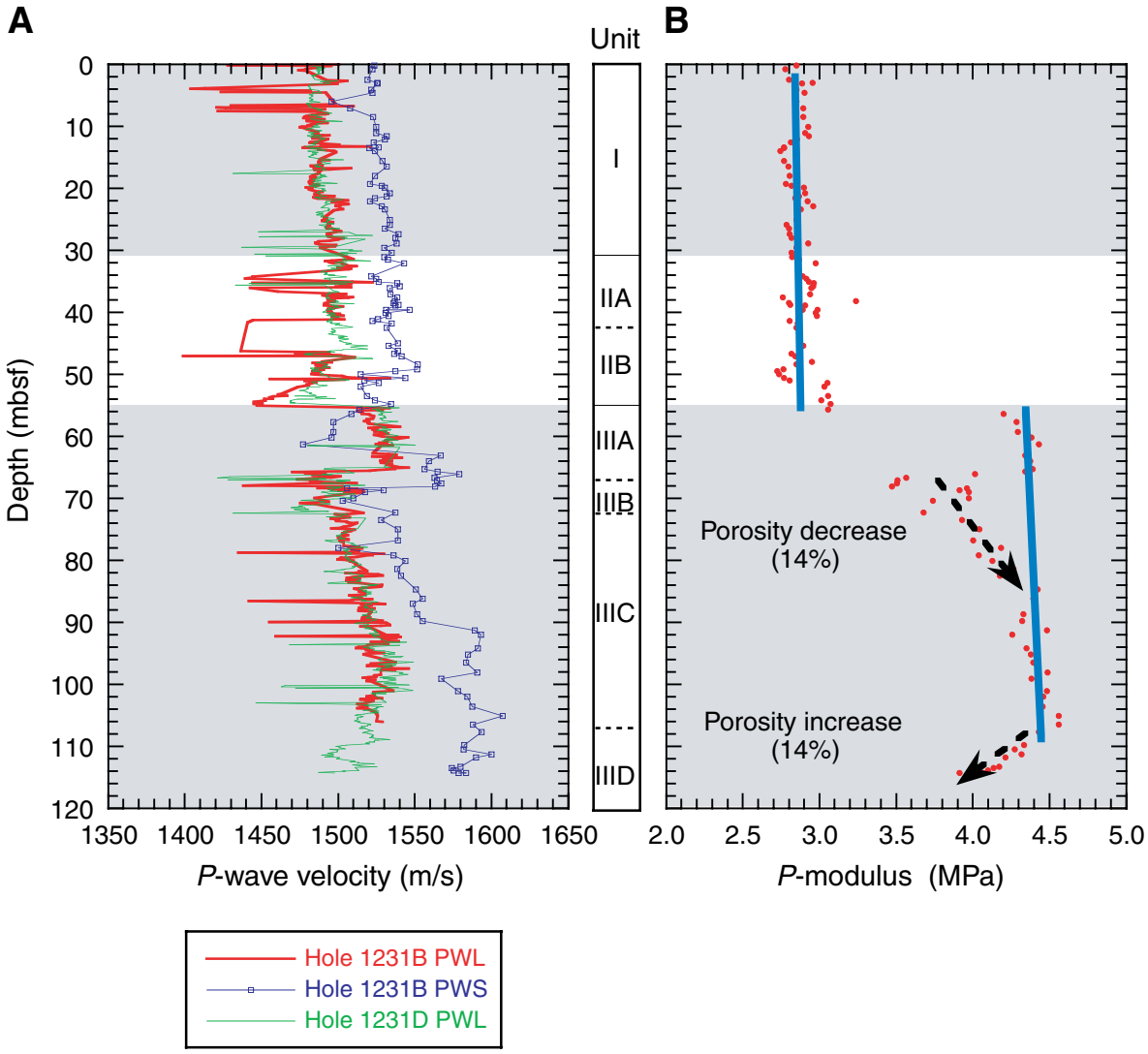

Figure F15. Natural gamma radiation (NGR) profiles for Holes 1231A to 1231D. Holes 1231B and 1231D detail the entire 0- to 114.5-mbsf sequence.

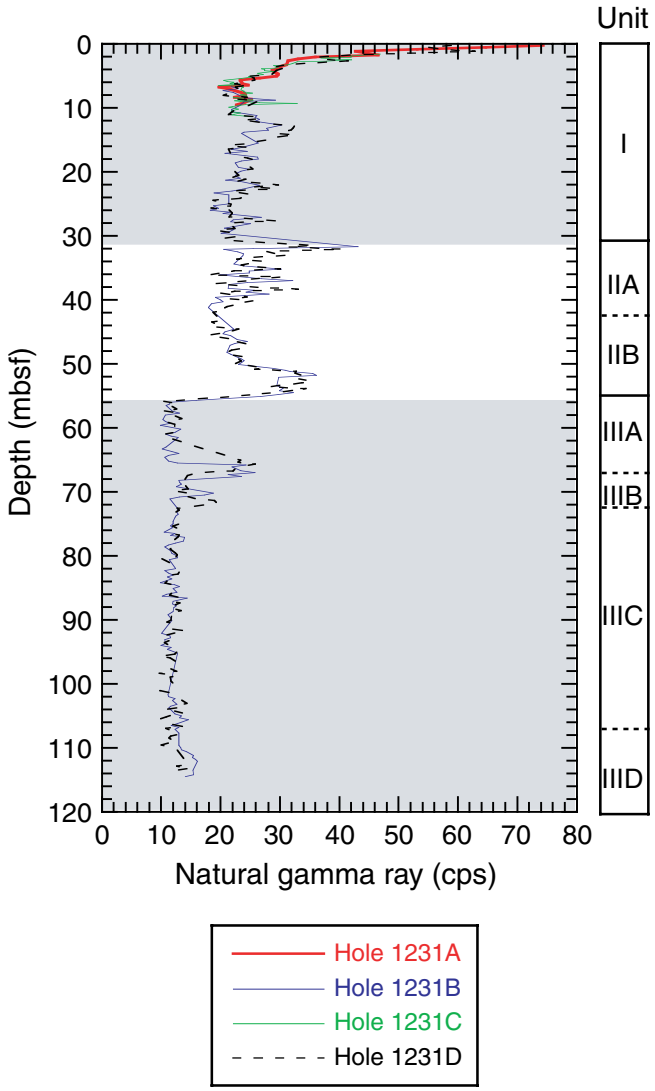

Figure F16. Formation factor profile for Hole 1231B. Trends (blue line) illustrate that porosity change is the dominant control on downhole electrical conductivity variation. The trend in Subunit IIB (red line) exhibits a counterintuitive formation factor-porosity relationship, probably explained by changing pore structure resulting from increasing clay and amorphous oxide content. The abrupt increase at ~114 mbsf mainly represents a diagenetic alteration by closing interpore pathways.

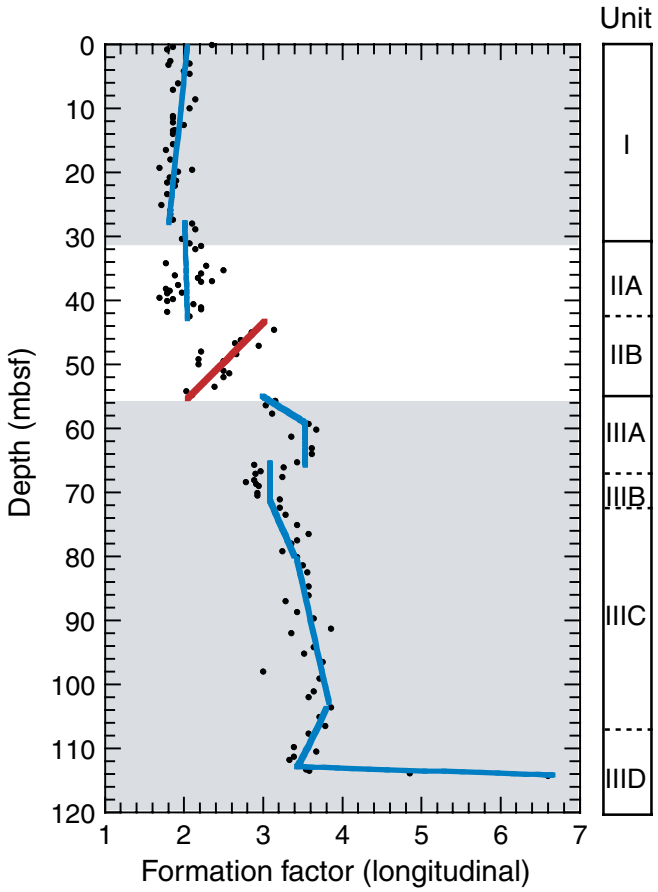

Figure F17. Thermal conductivity measurements for Holes 1231B, 1231D, and 1231E. **A.** Thermal conductivity profile (needle probe method). Note the abrupt thermal conductivity increase at the Unit II/III interface. **B.** Mean-detrended bulk density and thermal conductivity profiles illustrate the controlling effect of water content variability on thermal properties.

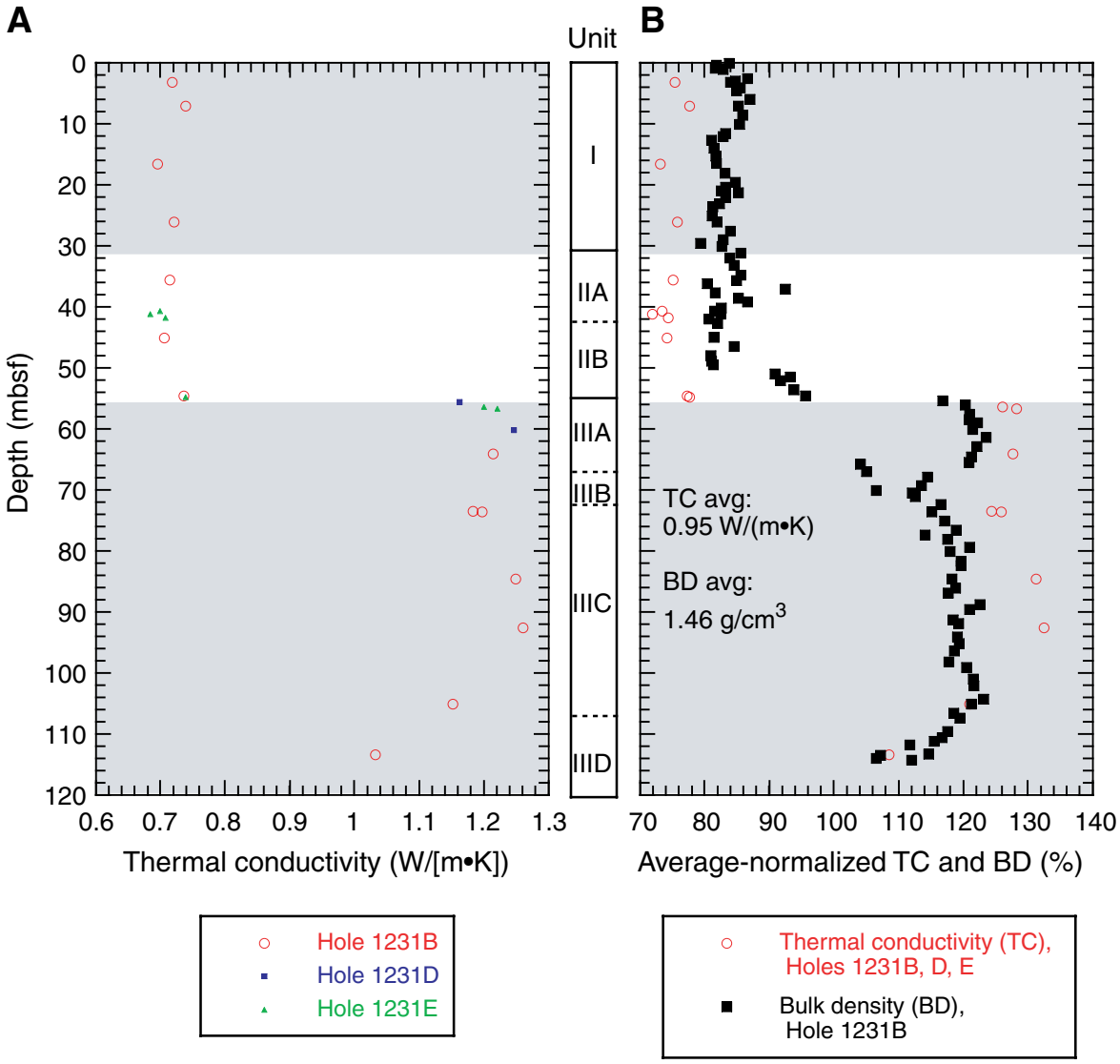

Figure F18. Temperatures measured in Holes 1231B, 1231D, and 1231E plotted vs. depth together with (**A**) best-fit linear profile for upper and lower sections and (**B**) Steady-state conductive profiles calculated using measured thermal conductivities from Hole 1231B and two values for uniform heat flow.

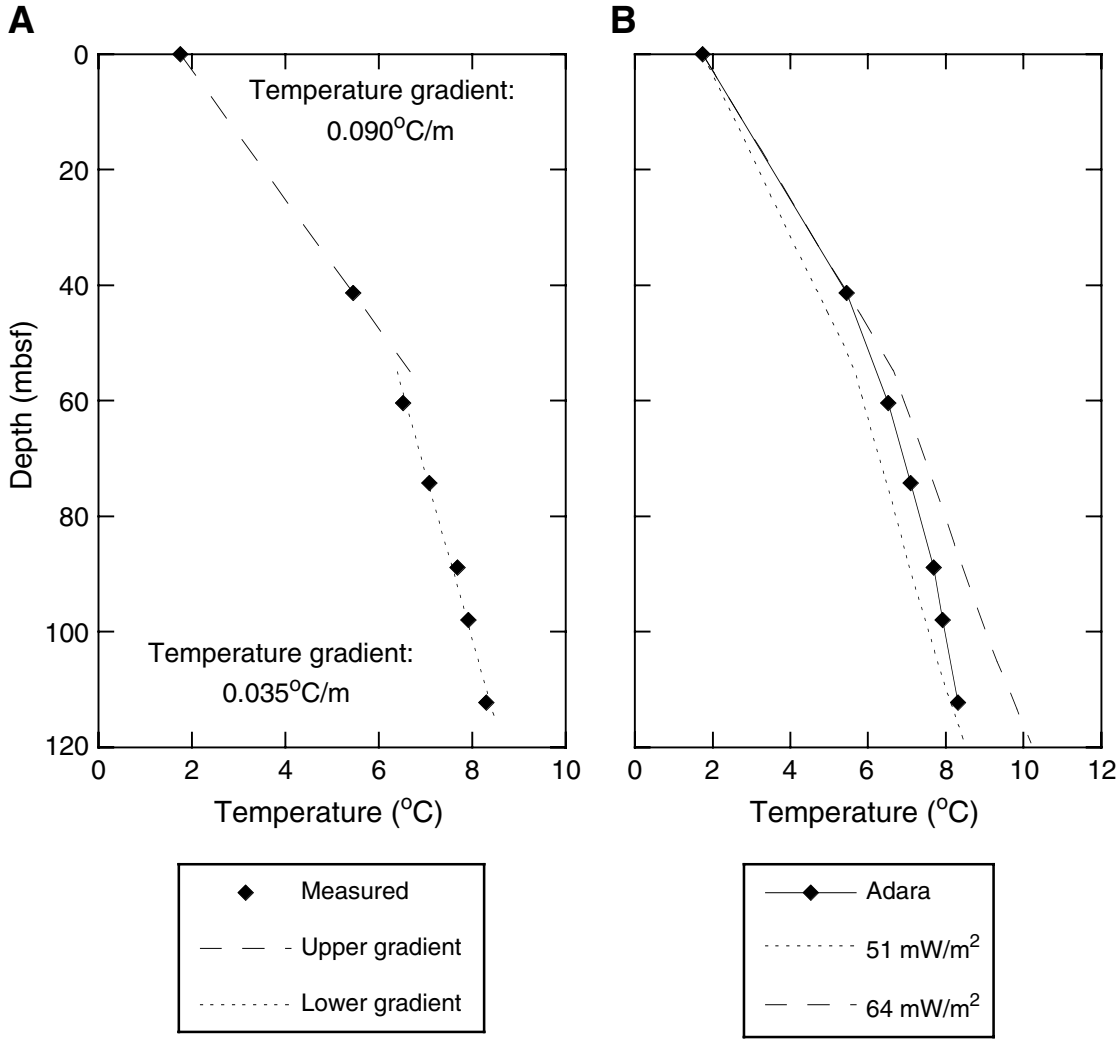

Figure F19. Pressure measured in Hole 1231B during the DVTP-P deployment after Core 201-1231B-12H.

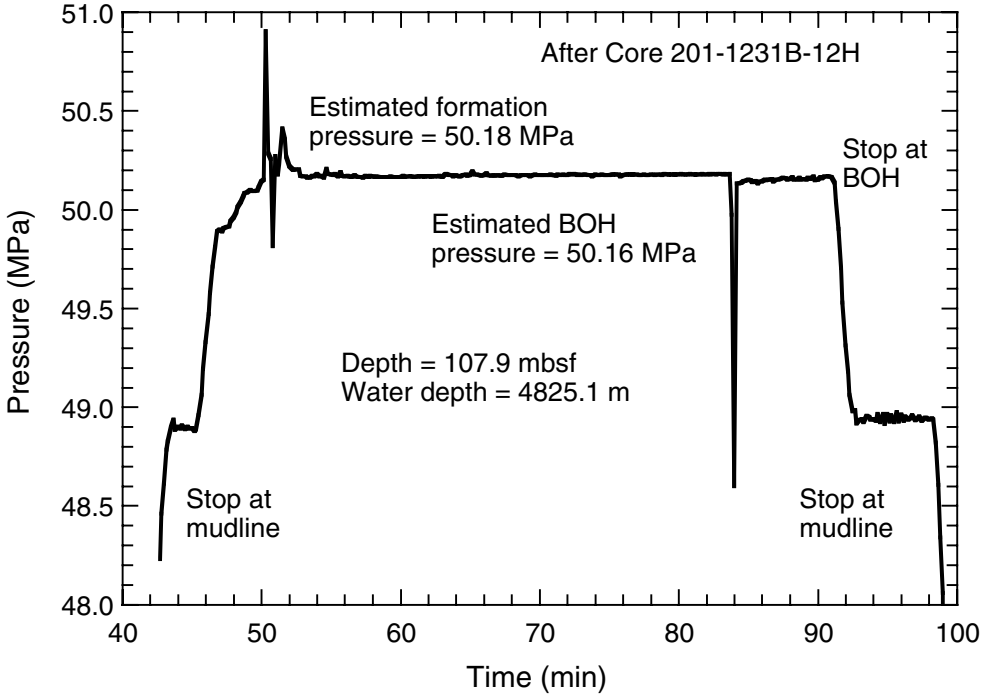

Table T1. Coring summary, Site 1231. (Continued on next page.)

Hole 1231A
Latitude: 12°1.2645′S
Longitude: 81°54.2413′W
Time on site (hr): 86.5 (0300 hr, 20 Mar–1730 hr, 23 Mar 2002)
Time on hole (hr): 9.17 (0300 hr, 20 Mar–1210 hr, 20 Mar 2002)
Seafloor (drill pipe measurement from rig floor, mbrf): 4824.0
Distance between rig floor and sea level (m): 11.4
Water depth (drill pipe measurement from sea level, m): 4812.6
Total depth (drill pipe measurement from rig floor, mbrf): 4833.5
Total penetration (meters below seafloor, mbsf): 9.5
Total length of cored section (m): 9.5
Total core recovered (m): 10.13
Core recovery (%): 106.6
Total number of cores: 1

Hole 1231B
Latitude: 12°1.2640′S
Longitude: 81°54.2393′W
Time on hole (hr): 27.83 (1210 hr, 20 Mar–1600 hr, 21 Mar 2002)
Seafloor (drill pipe measurement from rig floor, mbrf): 4825.1
Distance between rig floor and sea level (m): 11.4
Water depth (drill pipe measurement from sea level, m): 4813.7
Total depth (drill pipe measurement from rig floor, mbrf): 4942.4
Total penetration (meters below seafloor, mbsf): 117.3
Total length of cored section (m): 115.8
Total Length of drilled Intervals (m): 1.5
Total core recovered (m): 115.30
Core recovery (%): 99.6
Total number of cores: 14
Total number of drilled intervals: 1

Hole 1231C
Latitude: 12°1.2522′S
Longitude: 81°54.2400′W
Time on hole (hr): 2.42 (1600 hr, 21 Mar–1825 hr, 21 Mar 2002)
Seafloor (drill pipe measurement from rig floor, mbrf): 4823.9
Distance between rig floor and sea level (m): 11.4
Water depth (drill pipe measurement from sea level, m): 4812.5
Total depth (drill pipe measurement from rig floor, mbrf): 4839.0
Total penetration (meters below seafloor, mbsf): 15.1
Total length of cored section (m): 15.1
Total core recovered (m): 15.27
Core recovery (%): 101.1
Total number of cores: 2

Hole 1231D
Latitude: 12°1.2410′S
Longitude: 81°54.2410′W
Time on hole (hr): 20.58 (1825 hr, 21 Mar–1500 hr, 22 Mar 2002)
Seafloor (drill pipe measurement from rig floor, mbrf): 4823.7
Distance between rig floor and sea level (m): 11.4
Water depth (drill pipe measurement from sea level, m): 4812.3
Total depth (drill pipe measurement from rig floor, mbrf): 4945.6
Total penetration (meters below seafloor, mbsf): 121.9
Total length of cored section (m): 121.9
Total core recovered (m): 111.57
Core recovery (%): 91.5
Total number of cores: 13

Hole 1231E
Latitude: 12°1.2311′S
Longitude: 81°54.2392′W
Time on hole (hr): 26.5 (1500 hr, 22 Mar–1730 hr, 23 Mar 2002)
Seafloor (drill pipe measurement from rig floor, mbrf): 4823.9 mbrf
Distance between rig floor and sea level (m): 11.4
Water depth (drill pipe measurement from sea level, m): 4812.5
Total depth (drill pipe measurement from rig floor, mbrf): 4543.0
Total penetration (meters below seafloor, mbsf): 119.1
Total length of cored section (m): 119.1
Total core recovered (m): 118.57
Core recovery (%): 99.6
Total number of cores: 14

Table T1 (continued).

Core	Date (Mar 2002)	Local time (hr)	Depth (mbsf) Top	Depth (mbsf) Bottom	Length (m) Cored	Length (m) Recovered	Recovery (%)
201-1231A-							
1H	20	1210	0.0	9.5	9.5	10.13	106.6
				Cored totals:	9.5	10.13	106.6
201-1231B-							
1H	20	1310	0.0	3.4	3.4	3.40	100.0
2H	20	1425	3.4	12.9	9.5	9.62	101.3
3H	20	1550	12.9	22.4	9.5	9.74	102.5
4H	20	1700	22.4	31.9	9.5	10.04	105.7
5H	20	1840	31.9	41.4	9.5	10.01	105.4
6H	20	2130	41.4	50.9	9.5	9.93	104.5
7H	20	2315	50.9	60.4	9.5	9.54	100.4
8H	21	0030	60.4	69.9	9.5	9.18	96.6
9H	21	0220	69.9	79.4	9.5	9.76	102.7
10H	21	0400	79.4	88.9	9.5	9.65	101.6
11H	21	0535	88.9	98.4	9.5	9.51	100.1
12H	21	0735	98.4	107.9	9.5	9.65	101.6
			*****Drilled from 107.9 to 109.4 mbsf*****				
13H	21	1210	109.4	114.4	5.0	5.17	103.4
14X	21	1500	114.4	117.3	2.9	0.10	3.5
				Cored totals:	115.8	115.30	99.6
				Drilled total:	1.5		
				Total:	117.3		
201-1231C-							
1H	21	1715	0.0	5.6	5.6	5.64	100.7
2H	21	1825	5.6	15.1	9.5	9.63	101.4
				Cored totals:	15.1	15.27	101.1
201-1231D-							
1H	21	1935	0.0	7.8	7.8	7.76	99.5
2H	21	2045	7.8	17.3	9.5	9.51	100.1
3H	21	2200	17.3	26.8	9.5	9.80	103.2
4H	21	2315	26.8	36.3	9.5	9.82	103.4
5H	22	0020	36.3	45.8	9.5	9.73	102.4
6H	22	0150	45.8	55.3	9.5	9.53	100.3
7H	22	0310	55.3	64.8	9.5	6.77	71.3
8H	22	0450	64.8	74.3	9.5	8.68	91.4
9H	22	0615	74.3	83.8	9.5	9.63	101.4
10H	22	0800	83.8	93.3	9.5	9.77	102.8
11H	22	0910	93.3	102.8	9.5	8.71	91.7
12H	22	1130	102.8	112.3	9.5	9.46	99.6
13X	22	1400	112.3	121.9	9.6	2.40	25.0
				Cored totals:	121.9	111.57	91.5
201-1231E-							
1H	22	1610	0.0	3.0	3.0	5.71	190.3
2H	22	1710	3.0	12.5	9.5	9.13	96.1
3H	22	1820	12.5	22.0	9.5	9.46	99.6
4H	22	1925	22.0	31.5	9.5	9.88	104.0
5H	22	2030	31.5	41.0	9.5	9.55	100.5
6H	22	2130	41.0	50.5	9.5	9.93	104.5
7H	22	2235	50.5	60.0	9.5	9.52	100.2
8H	22	2340	60.0	69.5	9.5	9.81	103.3
9H	23	0050	69.5	79.0	9.5	9.62	101.3
10H	23	0150	79.0	88.5	9.5	8.99	94.6
11H	23	0410	88.5	98.0	9.5	9.95	104.7
12H	23	0515	98.0	107.5	9.5	5.03	53.0
13H	23	0645	107.5	117.0	9.5	9.90	104.2
14H	23	0800	117.0	119.1	2.1	2.09	99.5
				Cored totals:	119.1	118.57	99.6

Table T2. Comparison of basalt compositions from Site 321 (DSDP Leg 34) and Hole 1226B (ODP Leg 201). (See table notes. Continued on next page.)

Sample:	Site 321 average	201-1231B-14X-1, 0–2 cm	Standard BIR1	SRM reported value
Major element oxide (wt%):				
SiO_2	50.32	48.73	47.93	47.96
TiO_2	2.37	2.64	0.98	0.96
Al_2O_3	12.86	14.1	15.43	15.5
Fe_2O_3*	14.54	15.72	11.25	11.3
MnO	0.18	0.21	0.16	0.18
MgO	5.91	5.11	9.24	9.7
CaO	10.4	9.96	13.05	13.3
Na_2O	2.5	2.49	1.71	1.82
K_2O	0.17	0.53	0.02	0.03
P_2O_5		0.27	0.02	0.02
LOI		3	2	
Total	99.25	99.76	99.79	100.77
Trace element (ppm):				
Ba		18	7	7
Ni		41	147	170
Sc		43	40	44
Cr		89	356	370
Cu		70	116	125
Dy		9.85	2.61	4
Ce		18.1	3.7	1.9
Co		37.9	56.1	52
Eu		2.04	0.49	0.55
Gd		8.42	1.98	1.8
Hf		4.7	<0.5	0.6
Nd		17.8	2.7	2.5
La		7.3	0.8	0.63
Li				
Sr		103.3	108.7	110
V		472	337	310
Y		60.3	17.1	16
Zn		119	51	70
Zr		151.5	13.7	18
SRM informational values (ppm):				
As		1.5	0.6	0.44
B				
Be				
Cl				
F				
Ga		20.8	16.1	16
Lu		0.92	0.27	0.26
Nb		4.5	<0.5	0.6
Pb		0.8	4.5	3
Sb		0.1	0.5	0.58
Sm		6.7	1.2	1.1
Additional elements (ppm):				
C		0.04		
S		<0.01		
Mo		0.3	<0.1	
Cd		<0.1	<0.1	
Bi		<0.1	<0.1	
Ag		<0.1	<0.1	
Au (ppb)		6.8	2.4	
Hg		<0.01	<0.01	
Tl		0.1	<0.1	
Cs		0.5	<0.1	
Rb		11.5	<0.5	
Sn		2	<1	
Ta		0.4	<0.1	
Th		0.4	<0.1	
U		0.5	<0.1	
W		<0.1	<0.1	
Pr		3.21	0.41	
Ho		2.18	0.6	
Tb		1.49	0.37	

Table T2 (continued).

Sample:	Site 321 average	201-1231B-14X-1, 0–2 cm	Standard BIR1	SRM reported value
Er		6.65	1.78	
Tm		0.97	0.27	
Yb		6.32	1.61	

Notes: SRM = standard reference material., BIR-1 = USGS Icelandic basalt SRM, Leg 112 analyses are reported in Bunch and LaBorde (1976). Leg 201 analysis were conducted by inductively coupled plasma (ICP)–atomic emission spectrophotometry (major element oxides and Ba, Ni, Sc, and Cr) and ICP–mass spectrophotometry (all other trace elements). Leg 201 analysis were performed by Acme Labs, Vancouver, BC. The SRM was included in analytical suite as an unknown.

Table T3. Concentrations of dissolved species in interstitial waters, Holes 1231B and 1231E. (See table notes. Continued on next page.)

Core, section, interval (cm)	Depth (mbsf)	Alk (mM)	Cl^- (mM)	SO_4^{2-} (mM)	H_4SiO_4 (µM)	PO_4^{3-} (µM)	NH_4^+ (µM)	Fe (µM)	Mn (µM)	Sr (µM)	Li (µM)	Ba (µM)	ΣH_2S (mM)	DIC (mM)	Acetate (µM)	Formate (µM)	NO_3^- (µM)
201-1231B-																	
1H-1, 135–150	1.35	2.99	555.9	28.72	571	6.92	7,640	31.4	17.0	84	27.1	1.3		2.82	1.3	1.5	
1H-2, 135–150	2.85	3.17	557.9	28.49	685	5.33	17,010	35.2	25.3	85	26.6	0.7		2.88			
2H-1, 135–150	4.75	3.07	561.4	28.95	679	7.94		28.7	52.6	87	25.5	1.4		2.87	1.6	1.5	
2H-2, 135–150	6.25	3.12	562.4			11.14	30,520	13.2	60.0	86	25.1	0.4		3.01			
2H-3, 135–150	7.75	3.14	564.9	28.21	620	9.19	34,790	7.8	62.3	84	24.7	1.2		3.10			
2H-4, 135–150	9.25	3.12	565.9			8.00	32,720	12.6	68.7	85	25.2	0.9		3.08			
2H-5, 135–150	10.75	3.24	568.0	29.03		9.06		22.3	69.6	85	25.8	1.1	<0.0002	3.14			
2H-6, 135–150	12.25		571.0			6.24		6.8	71.5	85	25.6	0.4		2.68			
3H-1, 135–150	14.25	3.40	572.5	29.21	642	7.30	34,240	25.0	76.5	85	25.9	0.3		3.21			
3H-3, 135–150	17.25	3.44	570.0	29.16	664	6.33		17.9	78.3	86	25.2	0.8	<0.0002	3.23			
3H-5, 135–150	20.25	3.42	570.0	28.89		4.04	35,890	26.4	77.1	86	26.0	0.5		3.23			
4H-1, 135–150	23.75	3.41	569.0	28.57	647	2.53	32,580	24.7	80.5	90	26.5	0.3		3.24			
4H-3, 135–150	26.75	3.60	569.5	28.12	688	3.78	29,830	16.6	82.7	88	26.7	0.3	<0.0002	3.14	9.3	8.8	
4H-5, 135–150	29.75	3.43	570.0			4.72	33,410	8.9	92.3	88	25.9	0.4		3.19			
5H-1, 135–150	33.25	3.48	570.5	28.48	540	3.74	30,930	2.1	103.5	88	26.6	0.4		3.15			
5H-3, 135–150	36.25	3.48	571.5	28.49	614	2.64	30,520	0.9	118.9	88	26.0	0.3	<0.0002	3.18	3.6	8.9	
5H-5, 135–150	39.25	2.28	573.8	28.31		2.26	31,340	2.0	120.1	88	26.4	0.4		3.18			0.0
6H-1, 135–150	42.75	3.47		28.65	501	2.26	29,410	1.1	118.9	90	25.7	0.3		3.27	13.5	14.7	
6H-3, 135–150	45.75	3.46	572.5	28.54	495	2.26		1.4	119.8	90	25.8	0.3					
6H-5, 135–150	48.75	3.63		28.38		2.36	28,450	1.1	113.0	92	26.2	0.3		3.32			
7H-1, 135–150	52.25			27.75	443	1.77	30,240	2.0	93.1	87	26.1	0.6		3.59	6.9	6.8	
7H-3, 135–150	55.25	3.99	572.5	27.02	426	2.19	27,760	1.0	75.8	88	27.2	0.3	<0.0002	3.74			
7H-5, 135–150	58.25	3.59		27.88		2.17	23,760	1.1	50.8	85	26.2	0.4		3.34			1.7
8H-1, 135–150	61.75	3.56		27.60	329	1.31	22,660	1.6	24.9	89	26.1	0.3		3.28			
8H-3, 135–150	64.75	3.50	574.0	27.51	345	1.29	19,490	1.0	10.0	86	26.2	0.4	<0.0002	3.38			
8H-5, 135–150	67.75	3.61		25.87		1.93	21,840	1.1	0.3	87	26.8	0.3		3.17	13.2	13.8	
9H-1, 135–150	71.25	3.47		27.41	325	1.16		3.1	0.8	89	28.1	0.5		3.33			
9H-3, 135–150	74.25	3.71	573.5	26.92	345	2.81	9,020	5.0	0.2	87	28.4	0.5	<0.0002	3.27	6.0	14.9	
9H-5, 135–150	77.25	3.59		26.85		1.35	9,980	2.3	0.1	88	28.2	0.3		3.33			2.4
10H-1, 135–150	80.75	3.45		26.95	316	0.82	11,500	1.3	0.5	87	28.0	0.3		3.31	4.0	19.0	
10H-3, 135–150	83.75	3.37	572.5	27.22	337	1.07	13,150	2.1	0.0	88	28.8	0.3	<0.0002	3.25			
10H-5, 135–150	86.75	3.43		26.94		1.20	9,430	2.4	0.1	86	28.3	0.3		3.29			3.6
11H-1, 135–150	90.25	3.36		27.61	322	1.24	10,540	1.3	0.2	88	28.5	0.3		3.17	4.8	4.3	5.0
11H-3, 135–150	93.25	3.40	571.0	27.58	322	1.09		1.1	0.1	86	26.7	0.2	<0.0002	3.36			
11H-5, 135–150	96.25	3.37		27.48		1.07	5,300	1.2	0.1	87	27.6	0.2		3.23			
12H-1, 135–150	99.75	3.24		27.52	315	0.93	1,990	1.5	0.4	87	28.9	0.3		3.00			
12H-3, 135–150	102.75	3.77	571.0	27.13	362	1.13	1,440	1.1	0.2	87	30.4	0.3	<0.0002	3.45	2.6	5.9	7.9
12H-5, 135–150	105.75	3.20		27.28		1.09	0,060	2.9	0.2	88	29.7	0.2		3.05			
12H-6, 135–150	107.25	3.12		27.02		0.85	4,060	2.6	0.2	89	33.6	0.4		3.37			
13H-1, 135–150	110.75			25.89	302	1.18	0,060	0.0	0.2	87	35.6	0.3		3.00			14.5
13H-2, 135–150	112.25	2.99		26.58		0.85	1,580						<0.0002	3.03			17.9
13H-3, 135–150	113.75	3.13	571.8	26.78	331	1.24	1,170	3.1	0.2	88	40.3	0.4		2.93	4.3	3.4	14.9
201-1231E-																	
1H-1, 0–10	0.00	2.93				1.09		0.8	0.8	85	34.5	0.3		2.95			39.3
1H-1, 10–20	0.10	2.91						0.7	0.3	85	30.2	0.3		2.80			27.1
1H-1, 40–50	0.40	2.95						1.5	4.3	86	27.5	0.3		2.76			10.2
1H-1, 70–80	0.70	2.97						8.6	9.9	86	27.9	0.3		2.83			2.4
1H-1, 100–110	1.00	2.95						14.3	13.5	86	27.0	0.3		2.78			1.3

Table T3 (continued).

Core, section, interval (cm)	Depth (mbsf)	Alk (mM)	Cl^- (mM)	SO_4^{2-} (mM)	H_4SiO_4 (µM)	PO_4^{3-} (µM)	NH_4^+ (µM)	Fe (µM)	Mn (µM)	Sr (µM)	Li (µM)	Ba (µM)	ΣH_2S (mM)	DIC (mM)	Acetate (µM)	Formate (µM)	NO_3^- (µM)
3H-2, 70–80	14.70	3.29						15.7	75.5	88	25.2	0.2		3.33			
3H-2, 140–150	15.40	3.29						13.4	77.1	88	25.6	0.4		3.28			
3H-3, 70–80	16.20	3.37						13.8	78.5	88	25.3	0.3		3.07			
3H-3, 140–150	16.90	3.29						22.4	78.5	88	26.1	0.2		3.17			
10H-5, 140–150	86.28	4.09						1.0	0.1	86	27.7	0.3		3.64			1.3
11H-5, 135–150	95.85	3.67						0.9	0.8	88	26.7	0.3		3.33			0.3
12H-1, 135–150	99.35							1.0	0.3	85	27.1	0.3		3.25			1.8
12H-2, 135–150	100.85							1.2	0.5	86	28.5	0.4					1.9
12H-3, 135–150	102.35							2.2	0.1	88	29.1	0.3					0.4
13H-1, 135–150	108.85							2.2	0.1	89	29.9	0.3					1.7
13H-2, 135–150	110.35							1.0	0.1	92	35.3	0.2					5.3
13H-3, 135–150	111.85							1.4	0.2	90	32.6	0.4					1.5
13H-4, 135–150	113.35				346			1.5	0.2	90	33.9	0.3					2.8
13H-5, 135–150	114.85				359			1.3	0.1	88	34.8	0.3					5.4
13H-6, 135–150	116.35				364			1.8	0.1	89	40.8	0.2					4.0
14H-2, 78–94	118.29				341			1.9	0.3	93	30.9	0.3					11.6

Notes: Alk = alkalinity, DIC = dissolved inorganic carbon. This table is also available in **ASCII.**

Table T4. Oxygen concentrations by microelectrode, Hole 1231D.

Core, section, interval (cm)	Depth (mbsf)	Oxygen (µM)
201-1231D-		
1H-1, 18	0.18	127
1H-1, 40	0.40	86
1H-1, 60	0.60	40
1H-1, 80	0.80	<20
1H-1, 97	0.97	<20
1H-1, 120	1.20	<20
1H-2, 10	1.60	<20
1H-3, 10	3.10	<20
1H-4, 10	4.60	<20
12H-1, 75	103.55	<20
12H-3, 75	106.55	<20
12H-5, 75	109.55	36
13H-1, 75	113.05	92
13H-2, 75	114.55	157

Note: This table is also available in **ASCII.**

Table T5. Iron concentrations of replicate interstitial waters passed through different filters, Hole 1231E.

Core, section, interval (cm)	Fe (μM)	
	0.45-μm filter	0.02-μm filter
201-1231E-		
1H-1, 0–10	0.8	0.7
1H-1, 10–20	0.7	0.7
1H-1, 40–50	1.5	1.7
1H-1, 70–80	8.6	8.5
1H-1, 100–110	14.3	14.5
3H-2, 70–80	15.7	16.3
3H-2, 140–150	13.4	12.3
3H-3, 70–80	13.8	13.0
3H-3, 140–150	22.4	22.8
10H-5, 135–140	1.0	2.0
11H-5, 135–140	0.9	0.9

Note: This table is also available in **ASCII.**

Table T6. Hydrogen concentrations, Hole 1231B.

Core, section, interval (cm)	Depth (mbsf)	H_2 (nM)	Incubation temperature (°C)
201-1231B-			
1H-2, 85–91	2.35	49.10	4
2H-2, 85–91	5.75	28.58	4
3H-2, 65–71	15.05	102.30	4
4H-2, 50–56	24.40	61.66	4
5H-2, 50–56	33.90	6.62	4
6H-2, 90–96	43.80	0.05	4
7H-2, 50–56	52.90	0.07	4
8H-2, 35–41	62.25	0.13	4
9H-2, 55–61	71.95	0.05	4
10H-2, 50–56	81.40	0.22	4
11H-5, 105–111	95.95	0.18	4
12H-2, 80–86	100.70	0.04	4
13H-3, 50–56	112.90	0.13	4

Note: This table is also available in **ASCII.**

Table T7. Methane concentrations in headspace, Hole 1231B.

Core, section, interval (cm)	Depth (mbsf)	Methane (ppm in headspace) 20 min @ 60°C	1.5 days @ 22°C	2.5 days @ 22°C	Methane (µM)
201-1231B-					
1H-1, 130–135	1.30		1.7	18.3*	2.7
1H-2, 130–135	2.80	1.8			0.1
2H-1, 130–135	4.70		5.1	22.6*	3.5
2H-3, 130–135	7.70	2.0			0.1
2H-6, 130–135	12.20		14.2	79.4*	12.5
3H-1, 130–135	14.20		8.9	37.3*	5.7
3H-3, 130–135	17.20	2.1			0.1
3H-6, 145–150	21.85		12.8	78.3*	12.7
4H-1, 130–135	23.70		12.5	69.4*	10.8
4H-3, 130–135	26.70	2.2			0.1
4H-5, 130–135	29.70		31.4	89.7*	15.4
5H-1, 130–135	33.20		16.2	76.0*	12.4
5H-3, 130–135	36.20	2.0			0.1
5H-6, 0–5	39.40		13.8	73.8*	12.0
6H-1, 130–135	42.70		18.2	96.9*	15.1
6H-3, 130–135	45.70	2.1			0.1
6H-6, 0–5	48.90		2.6*	2.9	0.2
7H-1, 130–135	52.20		2.1*		0.1
7H-3, 130–135	55.20	2.1			0.2
7H-6, 0–5	58.40		2.1*	1.6	0.1
8H-3, 0–5	63.40		1.9*		0.1
8H-4, 0–5	64.90	1.7			0.0
8H-6, 0–5	67.90		1.8*	1.6	0.0
9H-1, 130–135	71.20		2.3*		0.2
9H-4, 0–5	74.40	1.6			0.0
9H-6, 0–5	77.40		1.8*	1.6	0.0
10H-3, 0–5	82.40		2.5*		0.2
10H-4, 0–5	83.90	1.5			0.0
10H-6, 0–5	86.90		1.8*		0.1
11H-1, 130–135	90.20	1.6			0.0
11H-6, 0–5	96.40		1.8*	1.8	0.0
12H-1, 130–135	99.70	1.6			0.0
12H-4, 145–150	104.35		1.9*		0.1
13H-1, 130–135	110.70	1.6			0.0
13H-3, 130–135	113.70		1.8*		0.0

Notes: * = used for concentration in interstitial water. This table is also available in **ASCII.**

Table T8. Level of seawater contamination expected in cores based on the concentration of PFT observed in sediment, Holes 1231B and 1231D.

Core, section	Sample details	ng PFT/ g sediment	Potential µL seawater/ g sediment
201-1231B-			
1H-2	Center	0.04	0.04
1H-2	Outside	0.05	0.05
2H-2	Center	0.01	0.01
2H-2	Outside	0.09	0.09
3H-2	Center	0.02	0.02
3H-2	Outside	0.19	0.19
6H-2	Center	BD	BD
6H-2	Outside	BD	BD
12H-2	Center (slurry)	0.03	0.03
13H-3	Center	0.03	0.03
13H-3	Outside	0.05	0.05
201-1231D-			
13X-CC	Center	0.03	0.03
13X-CC	Outside	1.24	1.24

Notes: Detection limit = 0.01 µL seawater/g sediment, BD = below detection. The potential for microbial contamination is based on 5×10^8 cells/L surface seawater. This may be viewed as an upper limit for microbial contamination because it requires the sediment be permeable enough to allow all of the contaminating cells to travel with the PFT.

Table T9. Potential seawater contamination for slurries based on PFT results, Hole 1231B.

Core, section	ng PFT/ mL slurry	Potential µL seawater/ mL slurry
201-1231B-		
1H-2	BD	BD
2H-2	BD	BD
6H-2	BD	BD
12H-5	BD	BD

Note: Detection limit = 0.025 µL seawater/mL slurry, BD = below detection.

Table T10. Media inoculated with sample material from different depths, Hole 1231B.

Core: Depth (mbsf):	1231B-1H 2	1231B-2H 5	1231B-6H 43	1231B-12H 101
Medium:				
Sed	15°C: MPN	15°C: MPN	15°C: MPN	15°C: MPN
Mono	15°C: MPN	15°C: MPN	15°C: MPN	15°C: MPN
Poly	15°C: MPN	15°C: MPN	15°C: MPN	15°C: MPN
Aro	15°C: MPN	15°C: MPN	15°C: MPN	15°C: MPN
Rad	4°C: MPN	4°C: MPN	4°C: MPN	4°C: MPN
Rad-Lac	4°C: MPN	4°C: MPN	4°C: MPN	4°C: MPN
Sed-SO_3	15°C: MPN	15°C: MPN	15°C: MPN	15°C: MPN
Mono-SO_3	15°C: MPN	15°C: MPN	15°C: MPN	15°C: MPN
Poly-SO_3	15°C: MPN	15°C: MPN	15°C: MPN	15°C: MPN
Past-Sed	15°C: MPN	15°C: MPN		
Past-Mono	15°C: MPN	15°C: MPN	15°C: MPN	15°C: MPN
Mono-O_2	15°C: MPN	15°C: MPN	15°C: MPN	15°C: MPN
Grad	15°C: EN	15°C: EN	15°C: EN	15°C: EN
SRB; 8.0	4°C, RT: DS, EN*			
201-1	RT, 50°C: EN	RT, 50°C: EN	RT, 50°C: EN	RT, 50°C: EN
201-2	50°C: MPN	50°C: MPN	50°C: MPN	50°C: MPN
Fe(III)red	10°C: EN	10°C: EN	10°C: EN	10°C: EN
Mn(IV)red	10°C: MPN	10°C: MPN	10°C: MPN	10°C: MPN

Notes: Enrichment assays were qualitative (EN) or quantitative (MPN) and incubated at the temperature given and/or at room temperature (RT = 21°–25°C). * = additional samples were taken from Cores 201-1231D-1H and 3H and 201-1231E-1H. Media are defined in Table **T9,** p. 90, in the "Explanatory Notes" chapter (see also **"Microbiology,"** p. 14, and Tables **T4,** p. 84, **T5,** p. 85, and **T7,** p. 88, all in the "Explanatory Notes" chapter).

Table T11. Downhole temperature measurement summary, Holes 1231A, 1231B, 1231D, and 1231E.

Depth (mbsf)	Tool used	Measurement location	Thermal conductivity (W/[m·K])	Temperature (°C)	Assessment
0.0	Adara	Seafloor, T Core 1231A-1H		1.75	Good
41.4	Adara	Core 1231B-5H	0.70	5.45	Good
60.4	Adara	Core 1231B-7H	1.25	6.52	Good
74.3	Adara	Core 1231D-8H	1.20	7.09	Good
88.9	Adara	Core 1231B-10H	1.26	7.69	Good
98.0	Adara	Core 1231E-11H	1.21	7.92	Good
112.3	Adara	Core 1231D-12H	1.05	8.44	Good
119.2	—	—	0.95*	8.63†	

Notes: T = top of core. * = average thermal conductivity. † = projected temperature at base of hole. The last line shows the temperature extrapolated to the base of the hole using linear fit of the lower portion in Figure **F18,** p. 49. — = not applicable.